3D Integrated On-Chip Wireless Power Delivery Interface

by

Salahuddin Raju

A Thesis Submitted to

The Hong Kong University of Science and Technology
in Partial Fulfillment of the Requirements for
the Degree of Master of Philosophy
in the Department of Electronic and Computer Engineering

August 2013

Authorization

I hereby declare that I am the sole author of the thesis.

I authorize the Hong Kong University of Science and Technology to lend this thesis to other institutions or individuals for the purpose of scholarly research.

I further authorize the Hong Kong University of Science and Technology to reproduce the thesis by photocopying or by other means, in total or in part, at the request of other institutions or individuals for the purpose of scholarly research.

Salahuddin Raju

Salahnddin Rojn

August 2013

3D Integrated On-Chip Wireless Power Delivery Interface

by

Salahuddin Raju

This is to certify that I have examined the above MPhil thesis and have found that it is complete and satisfactory in all respects, and that any and all revisions required by

the thesis examination committee have been made.

Professor Mansun J. CHAN, ECE, HKUST Thesis Supervisor

Professor C. Patrick YUE, ECE, HKUST Thesis Supervisor

Professor Philip K.T. MOK, ECE, HKUST Chairperson of Thesis Examination Committee

Professor Chi-Ying TSUI, ECE, HKUST Thesis Examination Committee Member

Professor Ross D. MURCH, ECE, HKUST Head of Department

Department of Electronic and Computer Engineering
Hong Kong University of Science and Technology
August 2013

Acknowledgments

I would like to express my heartfelt gratitude to my supervisors, Professor Mansun J. Chan and Professor C. Patrick Yue. Throughout my study, their patient guidance has helped me to develop a clear understanding of my research area. Without their supervision this work would have not been possible. Most importantly, their enthusiasm towards research has motivated me to move forward and challenge the boundaries of my work. They are my continuous inspiration.

It has been a great privilege for me to have Professor Philip K.T. Mok and Professor Chi-Ying Tsui on my thesis committee. Their insightful comments and suggestions have certainly benefited me in improving my work.

I would like to thank Dr. Rongxiang Wu. He has been a great support in every aspect of my project. It has been a pleasure to work with him. I am also grateful to Xing Li and Lu Yan for their continuous support and discussion to help me complete my project.

I want to show my gratitude to the stuff members of the HKUST Nanoelectronics Fabrication Facility for their assistance in wafer processing. Additionally, I would like to thank Allen, K.W. and Luk for their technical support.

Lastly, I want to thank my friends at the Device Characterization Laboratory and High Speed Silicon Laboratory for their help with training, experiments, and discussions: Lining Zhang, Ahmed Zubair, Aixi Zhang, Pan Quan, Yehan Chen, Swen Li, Li Sun and Zhengxiong Hou.

Table of Contents

Title Page	i
Authorization	ii
Signature Page.	iii
Acknowledgements	iv
Table of Contents	v
List of Figures.	vii
List of Tables.	x
Abstract	xi
Chapter 1 Introduction to wireless powering .	1
1.1 The necessity of wireless powering	1
1.2 Strategies of wireless powering	2
1.3 Challenges in integrated wireless powering scheme and solution	4
References	5
Chapter 2 Systematic modeling and analysis of the wireless power transfer interface	7
2.1 Wireless power transfer system and design parameters	7
2.2 Planar inductor modeling	9
2.3 Mutual coupling between planar inductors in wireless power applications	13
2.4 Wireless power link efficiency and voltage gain	27
2.5 Characterization of wireless power link and model verification	28
References	31
Chapter 3 Integrated wireless powering interface for sub-mm ² size SoC	35
3.1 Design considerations of an integrated wireless power link	35
3.2 Silicon embedded inductor technology	36
3.3 Above CMOS inductor (ACI) integration technique	41
3.4 Characterization of the wireless power link in bio-environment	46

References	50
Chapter 4 Demonstration of a complete wireless power transfer system	52
4.1 Detail measurement setup of the demonstration	52
4.2 Performance of the power transfer system	54
References	57
Chapter 5 Conclusion	59
5.1 Summary of contributions	59
5.2 Directions of future research	59

List of Figures

Figure 1.1: Strategies of wireless power transfer.
Figure 2.1: Physical (a) and electrical (b) configuration of a wireless power transmitting and receiving interface
Figure 2.2: Physical parameters of a planar inductor. (b) Lumped RLC model of the planar inductor
Figure 2.3: Measured <i>L</i> , <i>R</i> and <i>Q</i> of a planar inductor, and comparison between analytical calculation and measured results at different operating frequency. Here, $r_{out} = 10$ mm, $w = 250$ μ m, $t = 30$ μ m, $t = 30$ μ m, $t = 17$, and the shape of the inductor was square
Figure 2.4: (a) Concentric single turn coils and tracks were approximated as constant current carrying filaments to facilitate Neumann's integral for mutual inductance calculation. (b) Configuration of the filamentary coils with lateral displacement
Figure 2.5: (a) <i>M</i> at different separation distances using 3D EM simulation results and proposed model. (b) Comparison between the proposed model and the 3D EM simulation results in terms of error
Figure 2.6: (a) Variation of <i>M</i> with different coil radii and coil shapes, and (b) comparison with the numerical results.
Figure 2.7: Variation of <i>M</i> at different lateral displacements, and (b) comparison with a 3D EM simulation results.
Figure 2.8: Measurement setup for (a) PCB and PCB coils, (b) PCB and on-chip coil
Figure 2.9: Experimental extraction of inductances and maximum achievable efficiency for Link-3 at different operating frequency.
Figure 2.10: (a) Measured values of M at different axial separations between a planar PCB and PCB coils (Links-1 & 2); and (b) comparison with the predicted results in terms of error21
Figure 2.11: (a) Measured and predicted <i>M</i> due to lateral displacement at different axial distances for Link-1 (rectangular shaped PCB to PCB coils). (b) Comparison between measured and predicted results for Link-1. (c) Measured and predicted <i>M</i> due to lateral displacement for Link-2 (circular shaped PCB to PCB coils). (d) Comparison between measured and predicted results.
Figure 2.12: (a) Measured values of M at different axial separations between a planar PCB and on-chip coils (Links-3, 4 & 5); and (b) comparison with the predicted results
Figure 2.13: (a) Measured and predicted <i>M</i> due to lateral displacement at different axial distances for Link-3 (rectangular shaped PCB to rectangular shaped on-chip coils). (b) Comparison between measured and predicted results for Link-3. (c) Measured and predicted <i>M</i> due to lateral

displacement for Link-4 (circular shaped PCB to circular shaped on-chip coils), and (d) comparison between measured and predicted results
Figure 2.14: 3D simulation system of Link-3 in HFSS
Figure 2.15: Simplified schematic diagram of a wireless power link with lumped equivalent circuit elements
Figure 2.16: Maximum achievable efficiency at different operating frequency. Measurement was done both at 10 mm and 15 mm axial separations between primary and secondary inductor.
Figure 2.17: Maximum achievable efficiency at different axial separation while operating frequency fixed at 13.56 MHz
Figure 2.18: Variation of maximum achievable efficiency due to different lateral displacement while operating frequency was at 13.56 MHz
Figure 2.19: Measured efficiency and voltage gain at different load resistances. In this set of measurement frequency was at 13.56 MHz and relative axial distance between inductors fixed at 10 mm
Figure 3.1: Schematic 3D illustration of silicon embedded power receiving coil
Figure 3.2: (a) Cross-sectional view of embedded Cu tracks and vias obtained from a testing structure. (b) Bottom view of the fabricated 4.5×4.5 mm ² silicon-embedded receiving coil for wireless power transfer
Figure 3.3: Detail probing setup for two-port measurement of the wireless powering interface
Figure 3.4: Measured inductance and quality factor of the embedded power receiving inductor
Figure 3.5: Measured inductances of the embedded power receiving coil and the PCB transmitting coil along with their mutual inductances at different separation distances (at 5 mm and 12 mm).
Figure 3.6: Measured maximum achievable efficiency at different frequencies
Figure 3.7: Measured maximum achievable efficiency at different axial distances (a) and lateral displacements (b), while the operating frequency at 6.78 MHz
Figure 3.8: Variation of wireless power link with different load impedance, while the operating frequency was at 6.78 MHz, and the axial distance was at 10 mm
Figure 3.9: Schematic illustration of the major fabrication steps
Figure 3.10: (a) SEM images of trenches for the inductor which are filled by electroplated Cu. (b) Cross-sectional view of Cu tracks of the inductor. Over-plated Cu was removed by polishing. (c) Plane view of the fabricated inductor.

Figure 3.11: Measured inductance, quality factor and series resistance of the ACI integrated power receiving coil
Figure 3.12: Maximum achievable efficiency of the ACI integrated wireless power link at different frequencies
Figure 3.13: Maximum efficiency of the ACI integrated wireless power link at different axial distances
Figure 3.14: Measured link efficiency voltage gain of the ACI integrated wireless power link at different load resistances. These measurements were done at 10 mm axial distance
Figure 3.15: Experimental setup for measuring the wireless power link properties in bio- environment
Figure 3.16: Comparison between measured efficiency of the power link in air and bio- environment, while the spacing between the primary and the secondary coil was fixed at 5 mm
Figure 3.17: Comparison between quality factors obtained in air and bio-environment. Q_1 refers to the quality factor of the primary transmitting coil and Q_2 is for secondary power receiving coil
Figure 3.18: Variations in peak efficiency of the wireless power link in different operating environment (air or tissue) with various coupling distances. (a) Silicon embedded power receiving coil at the frequency of 6.78 MHz. (b) ACI integrated power receiving coil at the frequency of 13.56 MHz.
Figure 3.19: Comparison of the wireless power link efficiency with prior arts. SEI: Silicon Embedded Inductor, and ACI: Above-CMOS Inductor
Figure 4.1: Complete schematic diagram of a wireless power delivery system
Figure 4.2: (a) The chip micrograph of a retinal implant containing a rectifier and a secondary tuning capacitor ($C_R = 90$ pF) [7]. Area of the rectifier and the tuning capacitor are identified. Also, available space for above-CMOS inductor is also outlined, it is about 1.3×1.06 mm ² 53
Figure 4.3: A conceptual schematic diagram of the measurement setup53
Figure 4.4: The demonstration setup of the complete wireless power transfer system54
Figure 4.5: Time domain measurement of v_{in} , i_{in} and v_{DC}
Figure 4.6: Measured total system efficiency (η_{A-C}) at different frequencies

List of Tables

Table 1.1: Comparison among Different Strategies of Wireless Powering	3
Table 2.1: Modeling parameters for different kind of planar inductors	12
Table 2.2: Geometric Parameters of Wireless Power Links Constructed by Different Planar Inductors	
Table 2.3: Comparison of Simulation Efficiency	26
Table 3.1: Design Parameters of the Silicon Embedded Wireless Power Link	38
Table 3.2: Design Parameters of the ACI Integrated Wireless Power Link	44
Table 4.1: Parameters of Wireless Power Delivery Systems Constructed by Different Inductors	
Table 4.2: Comparison of Received Power Density among Different Type of Wireles Transmission Systems	

3D Integrated On-Chip Wireless Power Delivery Interface

by

Salahuddin Raju

Department of Electronic and Computer Engineering
The Hong Kong University of Science and Technology

Abstract

For system on a chip (SoC), a large value inductor (μ H) needs to be integrated within a sub-mm² area for the design of an efficient wireless power transfer interface. Integration of such a large value inductor is challenging and is beyond the scope of conventional integration techniques. This work outlines two CMOS compatible on-chip inductor integration approaches which can accommodate large value inductors without affecting the area of active circuitry. The first methodology implements the on-chip power receiving coil using silicon embedded inductor technology, in which inductors are fabricated in the thick bottom layer of the substrate. The second methodology integrates the inductor above the passivation layer of the CMOS chip. In both of these methodologies, no active circuitry is affected by the integration and effectively no extra area needs to be allocated for the inductor. Measurement results show that the fabricated inductors using these integration approaches can render a large quality factor (more than 20) with an inductance density of 200 nH/mm².

Alongside the integration techniques, a model of the wireless power link is required to design an efficient link which can transmit the maximum amount of power within the constraints of the application. This work presents a model of an inductive type near-field wireless power transfer interface to estimate its power efficiency and voltage gain. The proposed model does the prediction using the geometric variables of the system. Wireless power links were implemented, and the accuracy of the proposed model was confirmed by comparing the measured and calculated results. This model can also suggest the optimal operating frequency and load of an inductive link for maximal power transfer. In the end, utilizing the model and the integration techniques, efficient wireless power links, which can supply a mW range of power to sub-mm² bio-microsystems, were designed, with efficiency of more than 5% at an implantation depth of 10mm.

Chapter 1

Introduction to Wireless Powering

1.1 The necessity of wireless powering

Implanted biomedical devices have been of great assistance in monitoring biological parameters and for disease treatment of the human body. That's why in recent years, there has been significant progress in bio-microsystems which can perform a variety of bio-functionalities. For example, neural implants [1], [2] in the brain can sense neuron signals as well as stimulate the neuron. The thoughts of a person can be read by sensing the brain's neuron signals and, in future, this could be a means of communication for paralyzed persons. Some other examples of such bio-microsystems include retinal implants [3-6], endoscopic capsules [7], pacemakers [8] and cochlear implants [9]. As these devices are placed inside the body, an internal power source is required to deliver a certain amount of power to perform the bio-functionality. In the conventional approach, percutaneous wires and batteries are used to supply power to these devices. The use of percutaneous wires causes susceptibility to infections and is not suitable for long term application. Additionally, the short life span of batteries limits the energy budget of the bio-microsystem. As batteries contain hazardous materials, they also constitute a health risk. The conventional approach does not provide any permanent solution for powering bio-microsystems. An alternative means of powering is required for the safe and long term usage of these devices.

Considering the above mentioned issues, wireless power transfer is the most viable way to supply power to bio-microsystems as, in principle, available energy through wireless powering is infinite and there is no physical contact required for the transmission of power. The idea of wireless power transmission is 100 years old and was first proposed by Nikola Tesla [10]. However, researchers were not able to find a practical application of this idea until recent years. Applications like contactless battery charging platforms [11-14] and powering portable desktop peripherals [15] are commercially available, and these applications exploit the idea of wireless power transfer. Use of wireless powering for bio-microsystems is desirable to avoid the health risks associated with percutaneous wires and batteries and also to enable the miniaturization of

implantable bio-microsystems, ultimately leading to the safe and permanent application of these devices.

1.2 Strategies of wireless powering

In the literature, many strategies for wireless powering have been described. Based on the principle of electromagnetic (EM) field transmission, they can be categorized into three major classes, near-field, mid-field and far-field, as shown in Fig. 1.1. In the near field wireless power transfer system [16], [17], transmission distance and antenna dimensions are smaller than the wavelength. In practice, spiral inductors are used as the transmitting and receiving antennas. The transmitting inductor produces a time varying magnetic flux in the space. When the time varying magnetic flux passes through the receiving inductor, the flux induces voltage across the receiving side; thus power is transferred from the transmitting to the receiving side. This kind of wireless powering scheme is also known as inductive coupling. In the far field wireless transmission system [18], the antenna size is comparable to the wave length. The transmitting antenna radiates an EM wave into the surrounding media, and a remotely placed receiving antenna picks up a part of that EM radiated power; this is the basic working principle of far-field wireless powering. Using the far-field wireless transmission system, wireless power can be transmitted over a very large distance compared to the wavelength and the antenna dimensions. The mid-field wireless transmission system [19] works in between the near-field and far-field systems, and the transmission distance is comparable to the wavelength.

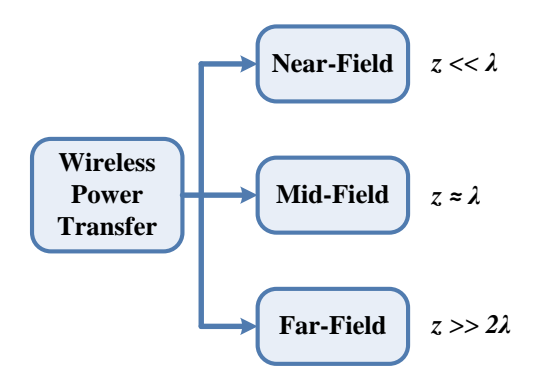


Figure 1.1: Strategies of wireless power transfer.

TABLE 1.1

COMPARISON AMONG DIFFERENT STRATEGIES OF WIRELESS POWERING

Strategy	Operating	Loss due	Efficiency	Directivity	Power	Transfer
	Frequency	to tissue			Range	Range, z
Near-field	Hz ~ 500MHz	No	High	Weak	~ W	Short
Mid-field	500MHz ~ sub GHz	Yes	Medium	Medium	~ sub mW	Medium
Far-field	~ GHz	Yes	Low	Strong	~ µW	Long

Every wireless power transmission system comes with its own criteria. The comparison among different kinds of wireless powering strategies is summarized in Table 1. For bio applications a suitable wireless power transfer scheme needs to be investigated. According to the demands of biomedical applications, the transfer range is several centimeters. For example, brain implants require an inter-coil distance of at least 5 mm (scalp thickness [20]) or 12 mm (scalp thickness + skull thickness [21]) and cardiac implants require a much higher axial distance of about 5 cm [22]. So, it is desirable to have a power transmission scheme which can supply a considerable amount of power with high efficiency. Typically, the near-field power transfer powering scheme provides higher transfer efficiency than the far-field.

Another major factor for selecting a suitable scheme for wireless powering is the operating frequency. For the mid-field and far-field wireless power transmission systems, the operating frequency resides in the sub-GHz and GHz range. The EM wave at these frequencies is absorbed by the muscle tissue. Because of this absorption, the EM wave attenuates inside the tissue environment. Also, this absorbed EM power dissipates as heat energy. Quantitatively, this phenomenon is expressed by the penetration depth at which the EM wave attenuates by a factor of 0.135. For an example, at 1GHz the penetration depth is about 3 cm. This lower penetration depth is one of the main reasons for lower transfer efficiency for mid-field and far-field wireless powering. If the wavelength is larger, the penetration depth is also larger. So, it is desirable to select a lower operating frequency so that the penetration depth is higher and loss due to the bio environment is less. For practical reasons, there is no requirement for directive wireless power transfer because the position of the implant is unknown when it is inside the body. Considering

all these issues, the near-field wireless powering scheme is the most suitable strategy for the wireless powering of bio-microsystems.

1.3 Challenges in the integrated wireless powering scheme and the solution

For practical reasons, miniaturization is the key trend for bio-microsystems. Miniaturized implants would be more comfortable and safe for patients. That's why there is an increasing interest in miniaturized bio-implants. For example, in a recently published work, a fully functional neural implant's size was only about $5\times5 \text{mm}^2$ [1]. To design a smaller bio-microsystem, the wireless power receiver should also be miniaturized. Also, there has been a research thrust to implement bio-microsystems on a single chip, i.e. system-on-chip (SOC), to reduce size, packaging complexity and to improve the system reliability as well. The main challenge of such a miniaturized power receiving system is to design a wireless power receiving inductor that can pick-up a sufficient amount of power to support the functionality of the implant.

It was mentioned earlier that near-field transmission is the most viable way to wirelessly power bio-implants. For biomedical applications, the industrial, scientific and medical (ISM) frequency band is dedicated at 6.78 MHz, 13.56 MHz, 27.12 MHz and 40.68 MHz. To design a wireless power transfer interface at the ISM frequency band, high inductance valued inductors (μH range) are required. Integration of this large value inductor with the bio-microsystem could serve the ultimate goal of miniaturization, and most importantly, it will reduce the total solution cost. Integration of a large value inductor within a sub-mm² area is challenging and beyond the scope of conventional integration techniques. This work outlines CMOS compatible on-chip inductor integration approaches which can accommodate large value inductors without affecting the area of active circuitry and ultimately create an efficient wireless powering interface for sub-mm² sized bio-microsystems.

In parallel to the integration, it is required to estimate the key parameters like power efficiency and voltage gain of the wireless power transfer interface. So, it is desirable to have a methodology to calculate the power link's performance parameters from the physical variables of the system. This work, addresses all these issues and presents a model of an inductive type near-field wireless power transfer interface that can estimate all these performance parameters. The

model also facilitates the design of an efficient wireless power transfer interface that can transmit the maximum amount of power within the constraints of the application.

References

- [1] R.R. Harrison *et al.*, "A low-power integrated circuit for a wireless 100-electrode neural recording system," *IEEE Journal of Solid-State Circuits*, vol. 42, no. 1, pp. 123-133, Jan. 2007.
- [2] W.J. Heetderks, "RF powering of millimeter- and submillimeter-sized neural prosthetic implants", *IEEE Transaciton on Biomedical Engineering*, vol. 35, no. 5, pp.323 -327, May 1988.
- [3] E. Zrenner, "Will Retinal Implants Restore Vision?" *Science*, Vol. 295 no. 5557 pp. 1022-1025, Feb. 2002.
- [4] C. Koch, W. Mokwa, M. Goertz, and P. Walter, "First results of a study on a completely implanted retinal prosthesis in blind humans," *IEEE Sensors Conference*, pp. 1237-1240, Oct. 2008.
- [5] L. Wu, Z. Yang, E. Basham, and W. Liu, "An efficient wireless power link for high voltage retinal implant," *IEEE Biomedical Circuits and Systems Conference*, pp. 101-104, Baltimore, MD, Nov. 2008.
- [6] G. Wang, et. al., "A dual band wireless power and data telemetry for retinal prosthesis," Annual International Conference of the IEEE Engineering in Medicine and Biology Society, New York, USA, 2006.
- [7] B Lenaer, and R. Puers, "An inductive power link for a wireless endoscope," *Biosensors and Bioelectronics*, Vol. 22, no. 7, pp. 1390-1395, Feb. 2007.
- [8] L. S. Y. Wong, S. Hossain, A. Ta, J. Edvinsson, D. H. Rivas, and H. Nääs, "A very low-power CMOS mixed-signal IC for implantable pacemaker applications," *IEEE Journal of Solid-State Circuits*, Vol.39, no. 12, Dec. 2004.
- [9] B. S. Wilson, et. al., "Better speech recognition with cochlear implants," *Nature*, vol. 352, pp. 236 238, July 1991.
- [10] N. Tesla, "Apparatus for transmitting electrical energy," U.S. Patent 1,119,732, Dec. 1, 1914.

- [11] E. Waffenschmidt, "Wireless power for mobile devices," *IEEE International Telecomunications Energy Conference*, Amsterdam, Oct. 2011.
- [12] H. Marques, and B. Borges, "Contactless battery charger with high relative separation distance and improved efficiency," *International Telecommunications Energy Conference*, Oct. 2011.
- [13] S. Y. R. Hui and W. C. Ho, "A new generation of universal contactless battery charging platform for portable consumer electronic equipment," *IEEE Transaction on Power Electronics*, vol. 20, no. 3, pp.620-627, May 2005.
- [14] W. X. Zhong, X. Liu and S. Y. R. Hui, "A novel single-layer winding array and receiver coil structure for contactless battery charging systems with free-positioning and localized charging features," *IEEE Transaction on Industrial Electronics*, vol. 58, no. 9, pp. 4136-4144, Sept. 2011.
- [15] P. Meyer, P. Germano, M. Markovic, and Y. Perriard, "Design of a Contactless Energy-Transfer System for Desktop Peripherals," *IEEE Transactions on Industry Applications*, vol. 47, no. 4, pp. 1643-1651 July/Aug 2011.
- [16] X. Liu and S. Hui, "Optimal design of a hybrid winding structure for planar contactless battery charging platform," *IEEE Transaction on Power Electronics*, vol.23, no.1, pp. 455-463, Jan 2008.
- [17] B. L. Cannon, J. F. Hoburg, D. D. Stancil and S. C. Goldstein, "Magnetic resonant coupling as a potential means for wireless power transfer to multiple small receivers," *IEEE Transactions on Power Electronics*, vol. 24, no. 7, pp.18191825, July 2009.
- [18] Z. Popovic´, et. al.,"Low-Power Far-Field Wireless Powering for Wireless Sensors," *Proceedings of the IEEE*, Vol.101, no. 6, pp. 1397 1409, June 2013.
- [19] J. S. Ho, S. Kim, and S. Y. Poon, "Midfield Wireless Powering for Implantable Systems," *Proceedings of the IEEE*, vol. 101, no. 6, pp. 1369 1378, June 2013.
- [20] H. Hori et al., "The thickness of human scalp: normal and bald," *Journal of Investigative Dermatology*, vol. 58, no. 6, pp. 396-399, 1972.
- [21] "Study: women's skulls thicker, men's wider; might affect protection design," Occupational Health & Safety, January 2008
- [22] S. Kim, J. S. Ho, L. Y. Chen, and A. S. Y. Poon, "Wireless power transfer to a cardiac implant," *Applied Physics Letters*, vol. 101, p. 073701, August 2012.

Chapter 2

Systematic modeling and analysis of the wireless power transfer interface

2.1 Wireless power transfer system and design parameters

The inductive type wireless power link is widely used for short distance wireless power transfer. A wireless power transfer system consists of a primary power transmitting coil and a secondary power receiving coil, which are both magnetically coupled. To estimate a power link's performance parameters (such as power efficiency, voltage gain, received power, etc.) or to design an optimized wireless power delivery system [1-7], a physical model of an inductive link is required. In this work, detailed derivations of these performance parameters, which include the prediction of the inductance (L), the resistance (R) and the quality factor (Q) of individual planar inductors, and the mutual inductance (M) between them, are described. As M depends on the shared magnetic field between the inductors, any change in axial and lateral displacement drastically changes M and thus power link performances as well. Also, any changes in the electrical load affect the efficiency and voltage gain of the link. So, it is desirable to have a methodology to calculate an inductive link's power efficiency and voltage gain from the geometric and electrical variables of the system.

One of the most reliable methods for computing L and Q of individual inductors and M between them is a 3D electromagnetic (EM) field solution [8]. However, simulation of the complex geometric system of a wireless power link in a 3D EM solver requires a lot of computational efficiency and time. Again, in the literature, various other approaches have been reported [2], [6]. However, these approaches do not include variation of the power efficiency and voltage gain according to different lateral misalignments and load resistances. In this work, all these performance affecting variables have been taken into account and an analytical model for predicting power efficiency and voltage gain is presented. The proposed model does the prediction from the geometric parameters of the planar coils, the relative placement of the coils and the electrical load of the inductive link. Thus, the proposed prediction methodology will

render a design procedure for the inductive link for maximum power transfer or an optimization technique for the specific type of application.

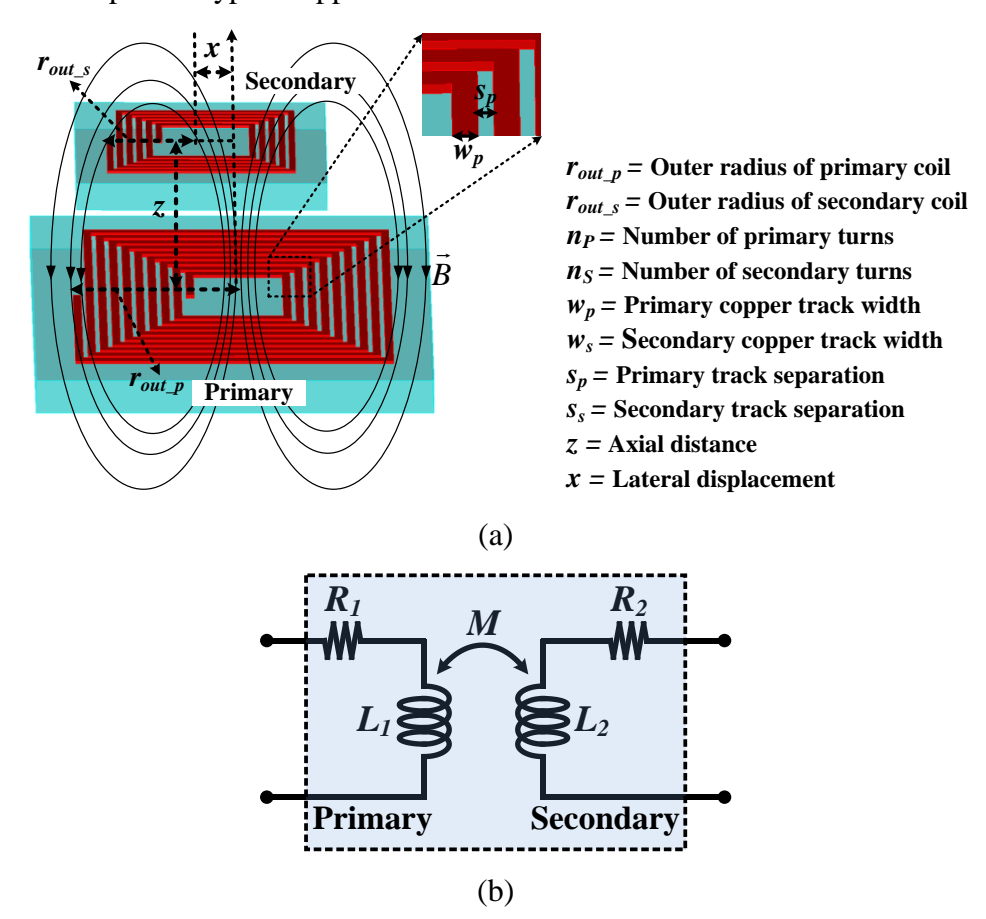


Figure 2.1: Physical (a) and electrical (b) configuration of a wireless power transmitting and receiving interface.

An inductive power link and its geometric parameters are described in Fig. 2.1(a), and its lumped equivalent circuit elements are shown in Fig. 2.1(b). The lumped inductance and resistance of the transmitting inductor are defined as L_1 and R_1 , and for the receiving inductor they are L_2 and R_2 respectively. In the subsequent text, physical models for predicting L_1 , R_1 , L_2 , R_2 and M are described in order to estimate a link's power efficiency and voltage gain.

2.2 Planar inductor modeling

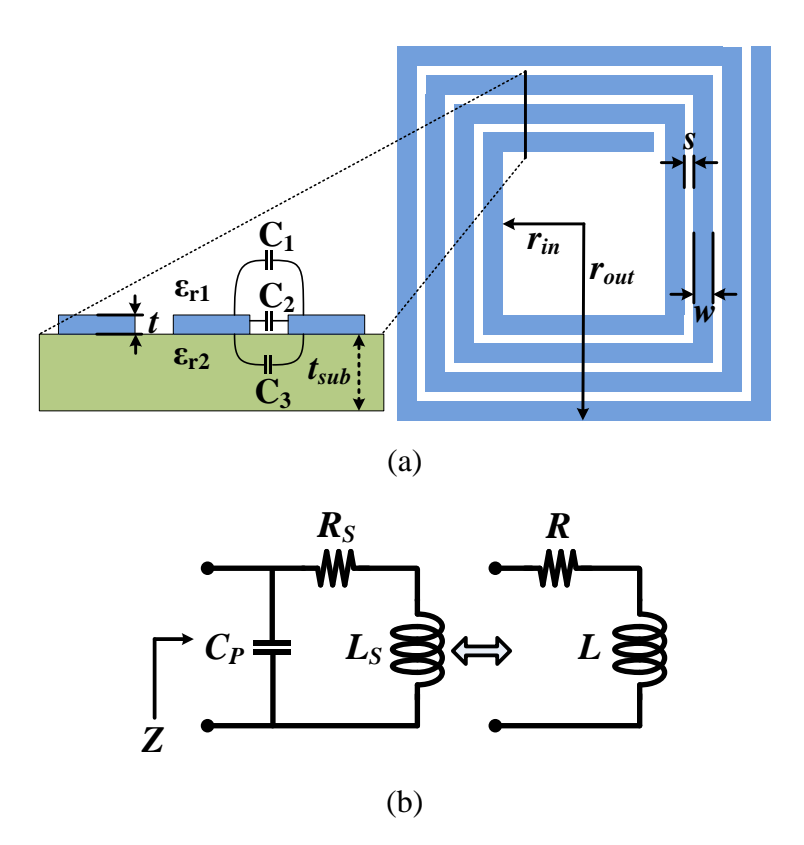


Figure 2.2: (a) Physical parameters of a planar inductor. (b) Lumped RLC model of a planar inductor.

The physical parameters of a planar inductor are described in Fig. 2.2(a). Here, the outer and inner radii are r_{out} and r_{in} , respectively. The track width, separation and thickness are defined as w, s and t, and n is the number of turns of the planar coil. The windings of the planar coil have parasitic resistance and capacitance, which are represented as lumped components, as indicated in Fig. 2.2(b). Here, the lumped resistance and capacitance are defined as R_S and C_P , and the total inductance is defined as L_S .

2.2.1 Modeling of inductance

The self inductance of an inductor is defined as the ratio between the magnetic flux produced by the current carrying tracks and the current passing through it. For a planar spiral inductor, a closed form expression [9] for the inductance can be represented as

$$L_{S} = \frac{c_{1} \mu n^{2} (r_{out} + r_{in})}{2} \left[\ln \left(\frac{c_{2}}{\varphi} \right) + c_{3} \varphi + c_{4} \varphi^{2} \right], \tag{2.1}$$

where, $\varphi = (r_{out} - r_{in})/(r_{out} + r_{in})$ and μ is the permeability of the metal in H/m. Here, parameters c_1 , c_2 , c_3 and c_4 depend on the shape/layout of the inductor [9], and these are described in Table 2.1.

2.2.2 Capacitance

The origin of the parasitic capacitance of a planar inductor is described in Fig. 2.2(a). Capacitors form between two parallel metal tracks of the inductor. The dielectric property of the insulating material (ε_{rl}) in which the metal tracks reside, the substrate (ε_{r2}) and the track separation determine the value of these capacitances. In this work, ε_{rl} and ε_{r2} are equal to 1 and 4.1 respectively. The value of the capacitance also depends on the track thickness and total length of the gap. For a square shaped inductor, the total length of the gap can be calculated as

$$l_{gap} = 4(2r_{out} - nw)(n-1) - 4n(n+1)s.$$
(2.2)

And the total capacitance can be estimated as

$$C_P = (C_1 + C_2 + C_3) \approx \left(\varepsilon_{r_1} + \alpha(\varepsilon_{r_1} + \varepsilon_{r_2})\right) \varepsilon_0 \frac{t}{s} l_{gap}, \qquad (2.3)$$

where, $\alpha = w/(w+s)$. This approach is adopted from [2].

2.2.3 Series resistance

The resistivity (ρ_c) of the metal, metal track thickness t, width w, and total length of the metal track (l_{total}) are required to calculate the dc resistance of a planar inductor. For a square shaped inductor, the total length of the metal track can be calculated as

$$l_{total} = 4n(2r_{out} - w - (n-1)(w+s)).$$
(2.4)

Under DC conditions, the total resistance can be determined as

$$R_{DC} = \rho_c \frac{l_{total}}{w t}. {(2.5)}$$

However, at a higher operating frequency the resistance increases due to the skin effect, and the AC resistance can be calculated as

$$R_{skin} = R_{DC} \frac{t w}{(w+t) \delta(1-e^{-t/\delta})}, \ \delta = \sqrt{\frac{\rho_c}{\pi \mu f}},$$
 (2.6)

where, δ is the skin depth and f represents the operating frequency in Hz.

To increase the mutual inductance between the planar inductors in a wireless power link, a higher turn number n is desirable and the coil tracks should fill all the way toward the center of the planar inductor, i.e. the r_{in}/r_{out} ratio is small. In this configuration the current crowding effect becomes dominant in the resistance estimation. When magnetic flux produced by the outer tracks penetrates the surface of the inner tracks, it creates an eddy current. This eddy current opposes the original current flow, and increases the resistance of the planar inductor [10]. This effect is more dominant in a planar inductor with a smaller r_{in}/r_{out} ratio. The increase in the resistance due to the current crowing effect can be expressed as

$$R_{crowd} = \frac{1}{2} \left(\frac{2\pi f}{w_{crit}} \right)^{2} \sum_{m=1}^{m=N_{e}} R_{sheet} \frac{l_{m}}{w} \left(\frac{m-M}{n-M} \right)^{2},$$

$$w_{crit} = \frac{3.1}{\mu_{0}} \frac{w+s}{w^{2}} \frac{\rho_{c}}{t}, \ l_{m} = r_{in} + \frac{w}{2} + (m-1)(w+s),$$
(2.7)

where, $N_e = n(1-r_{in}/r_{out})$, M = n/4, w_{crit} is defined as the frequency at which the current crowing effect becomes significant [10] and R_{sheet} (ρ_c/t) is defined as the sheet resistance of the metal.

By considering all these effects, the series resistance of a planar inductor can be determined as

$$R_{S} = R_{skin} + R_{crowd}. (2.8)$$

2.2.4 Quality Factor

Using (2.1) - (2.8), the impedance of a planar inductor can be calculated as

$$Z = \left(\frac{1}{j\omega C_P}\right) \| \left(R_S + j\omega L_S\right). \tag{2.9}$$

Here, R and L are defined as Re(Z) and Im(Z) respectively. The quality factor Q can be determined as

$$Q = \frac{\omega L}{R}.$$
 (2.10)

The proposed model is valid both for square and circular shaped inductors. However, some modeling parameters need to be changed according to the shape/layout of the inductor.

Necessary modeling parameters for square and circular shaped inductors are summarized in Table 2.1.

TABLE 2.1

MODELING PARAMETERS FOR DIFFERENT KINDS OF PLANAR INDUCTORS

Parameter	Square Shaped Inductor	Circular Shaped Inductor
c_1	1.27	1.00
<i>c</i> ₂	2.07	2.46
<i>C</i> ₃	0.18	0.00
C4	0.13	0.20
l_{gap}	$4(2r_{out}-nw)(n-1)-4n(n+1)s$	$\pi[(n-1)(2r_{out}-2w-s)-2(n-2)(n-1)(w+s)]$
l_{total}	$4n(2r_{out}-w-(n-1)(w+s))$	$\pi n \left[2r_{out} - w - (n-1)(w+s) \right]$

2.2.5 Experimental verification of the inductor model

To validate the proposed model experimentally, planar spiral inductors were implemented and 1-port s-parameter measurements were performed using an R&S ZVB8 vector network analyzer (VNA). These 1-port s-parameters were converted to a Z_{II} -parameter. At a specific frequency, L_I , and R_I were evaluated as $Im(Z_{II})$ and $Re(Z_{II})$ respectively. A sample of the measured inductance, resistance and quality factor $(L_I, R_I \text{ and } Q_I)$ is plotted in Fig. 2.3 and compared with the predicted results. Equation (2.1) - (2.10) was used to calculate these parameters.

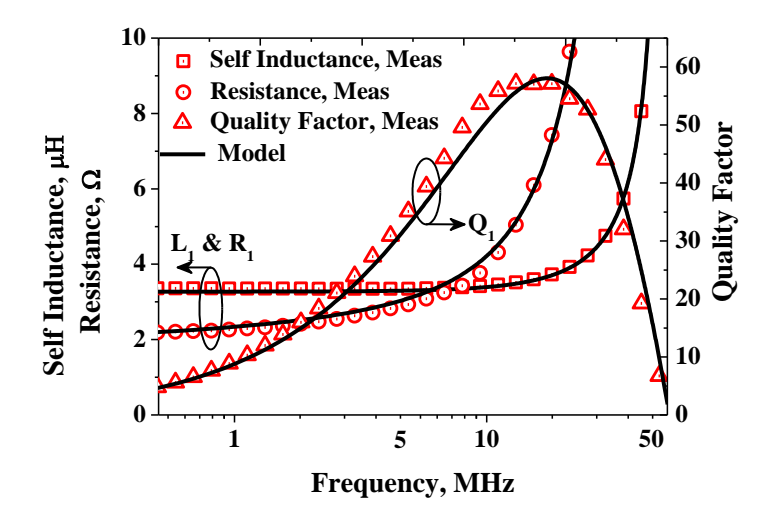


Figure 2.3: Measured *L*, *R* and *Q* of the planar inductor and comparison between the analytical calculation and measured results at different operating frequencies. Here, $r_{out} = 10$ mm, w = 250 µm, t = 30 µm, t = 30 µm, t = 17, and the shape of the inductor was square.

2.3 Mutual coupling between planar inductors in wireless power applications

In the literature, various approaches have been reported to compute mutual inductance (M), and most of these approaches are based on the look up table [11] and the numerical integration of elliptical [11]-[15] or Bessel functions [16]-[18]. Because of these numerical operations, computational complexity does not reduce. To design and optimize a wireless power transmission system, a compact analytical model of M is required. In this work, a compact model for predicting M, which does not need any numerical techniques, is presented. The proposed model does the prediction from the geometric parameters of the planar coils and the relative placement of the coils in the wireless power transmission system.

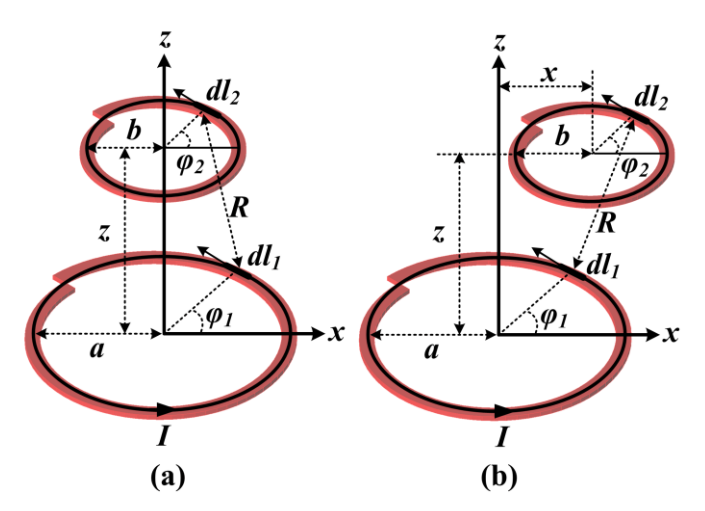


Figure 2.4: (a) Concentric single turn coils and tracks were approximated as constant current carrying filaments to facilitate Neumann's integral for mutual inductance calculation. (b) Configuration of the filamentary coils with lateral displacement.

2.3.1 Analytical model of mutual inductance

To calculate M, the tracks of the planar inductors are assumed as constant current carrying filaments [19], as shown in Fig. 2.4(a). M primarily depends on the geometric parameters of the inductors and their relative placement. For the basic analysis, it is assumed that the radius of the

primary coil is *a*, the secondary coil radius is *b*, the distance between these two concentric coils is *z*, and the turn number for both of them is *unity*. Neumann's equation is employed to calculate *M* between these two current carrying filaments [11]. *M* between two concentric filaments can be computed by the following equation:

$$M = \frac{\mu_0}{4\pi} \oint \int \frac{1}{R} d\vec{l_1} \cdot d\vec{l_2}, \qquad (2.11)$$

where $R = \sqrt{a^2 + b^2 + z^2 - 2ab \cos(\varphi_1 - \varphi_2)}$. By introducing the parameter $\gamma = 2ab/(a^2 + b^2 + z^2)$, M can be expressed as follows:

$$M = \frac{\mu_0 ab}{2\sqrt{a^2 + b^2 + z^2}} \int_{\varphi=0}^{\varphi=2\pi} \cos(\varphi_1 - \varphi_2) \left[1 - \gamma \cos(\varphi_1 - \varphi_2) \right]^{-1/2} d\varphi_1 . \tag{2.12}$$

For wireless power applications, the distance between the transmitting and receiving coils is typically large in comparison to the radius of the coil. Hence, the value of γ is much less than unity. For simplification, the $[1-\gamma\cos(\varphi_1-\varphi_2)]^{-1/2}$ term in (2.12) can be expanded up to the 7th order, as the rest of the term approaches to zero; thus, those higher order terms can be ignored. For example, if a=b and z=2a, the value of γ is equal to 0.5 and $\gamma^8\approx 0$, and the error incurred for this simplification is merely 0.038%, with comparison to the exact solution of Neumann's equation [11]. Using the above mentioned assumptions, M can be further simplified from (2) to

$$M = \frac{\mu_0 \pi \, a^2 b^2}{2(a^2 + b^2 + z^2)^{3/2}} \left(1 + \frac{15}{32} \, \gamma^2 + \frac{315}{1024} \, \gamma^4 \right). \tag{2.13}$$

However, if the coil separation is very large ($z >> r_{min}$, where r_{min} = the minimum radius of the coil among the primary and secondary), γ^2 and γ^4 will also diminish towards *zero*, and the equation can be further reduced to

$$M = \frac{\mu_0 \pi \, a^2 b^2}{2(a^2 + b^2 + z^2)^{3/2}}.$$
 (2.14)

It can be inferred from (2.14) that M is proportional to the area covered by each filament, and it is inversely proportional to the volume encompassed by the overall system.

The configuration of the planar coils for lateral displacement is shown in Fig. 2.4(b). Lateral displacement is represented by the parameter x. In this case, the cylindrical symmetry between

the two coils is lost, and the distance between two arbitrary points on the coils is presented as

$$R = \sqrt{a^2 + b^2 + z^2 + x^2 - 2ab\cos(\varphi_1 - \varphi_2) + 2xb\cos\varphi_2 - 2xa\cos\varphi_1}.$$

To calculate M, Neumann's equation is also employed in this case [37]. Let us introduce parameters $\gamma = 2ab/(a^2+b^2+z^2+x^2)$, $\alpha = 2xa/(a^2+b^2+z^2+x^2)$ and $\beta = 2xb/(a^2+b^2+z^2+x^2)$; M can be expressed as

$$M = \frac{\mu_0 ab}{4\pi\sqrt{a^2 + b^2 + z^2 + x^2}} \int_{\varphi_2 = 0}^{2\pi} \int_{\varphi_1 = 0}^{2\pi} \cos(\varphi_1 - \varphi_2) \left[1 - \left(\gamma \cos(\varphi_1 - \varphi_2) + \alpha \cos\varphi_1 - \beta \cos\varphi_2 \right) \right]^{-1/2} d\varphi_1 d\varphi_2. \quad (2.15)$$

For simplification, the $[1-(\gamma\cos(\varphi_1-\varphi_2)+\alpha\cos\varphi_1-\beta\cos\varphi_2)]^{-1/2}$ term in (2.15) can be expanded to the 5th order as the rest of the higher order term approaches towards *zero*. For example, if a=b,z=2a and x=a/2, the value of α is equal to 0.16 and α^6 approaches towards zero. In a similar manner, γ^6 and β^6 approach towards zero as well. Using this assumption, (2.15) can be solved as

$$M = \frac{\mu_0 \pi a^2 b^2}{2(a^2 + b^2 + z^2 + x^2)^{3/2}} \left[1 - \frac{3}{2} \delta + \frac{15}{32} \gamma^2 \left(1 - \frac{21}{2} \delta \right) + \frac{15}{16} \left(\alpha^2 + \beta^2 \right) \left(1 - \frac{7}{4} \delta \right) \right], \tag{2.16}$$

where $\delta = x^2/(a^2+b^2+z^2+x^2)$. Equation (2.16) can be used to estimate M for different lateral displacements at different axial separations.

Planar inductors have different shapes, turn numbers, coil widths and coil separations, as shown in Fig. 2.1. These are the necessary geometric parameters to calculate M between planar inductors. The outer radii are r_{out_p} and r_{out_s} , and the track widths are defined as w_p and w_s . The track separations are defined as s_p and s_s , and s_s , and s_s are the number of turns for the primary and secondary inductor, respectively. To estimate the s_s between planar inductors, it is a requirement to find all of the possible combinations of s_s by assuming each turn as a circular filament. And finally, total s_s can be determined by adding all these combinations of s_s . For different axial separations, the equation can be expressed as

$$M = \rho \times \sum_{i=1}^{i=n_p} \sum_{j=1}^{j=n_s} M_{ij} \text{ and } M_{ij} = \frac{\mu_0 \pi a_i^2 b_j^2}{2(a_i^2 + b_j^2 + z^2)^{3/2}} \left(1 + \frac{15}{32} \gamma_{ij}^2 + \frac{315}{1024} \gamma_{ij}^4\right), \tag{2.17}$$

where $a_i = r_{out_p} - (n_i - 1)(w_p + s_p) - w_p/2$, $b_j = r_{out_s} - (n_j - 1)(w_s + s_s) - w_s/2$ and $\gamma_{ij} = 2a_i b_j/(a_i^2 + b_j^2 + z^2)$.

Here, parameter ρ depends on the shape of the planar coils. If both the primary and secondary planar coils are circular shaped, $\rho = I$. Again, both of the coils can be rectangular shaped. The

area of a rectangular shaped coil having one side length of 2r possess a $4/\pi$ times larger area than a circular shaped coil with a diameter of 2r. According to (2.14), M is proportional to the area covered by each filament. Thus M between rectangular coils is $(4/\pi)^2$ times larger than between circular coils, i.e., $\rho = (4/\pi)^2$. However, if the area of one rectangular coil is very small compared to another, the smaller rectangular coil acts as a point source, i.e., a circular shaped coil, and parameter ρ can be described as

$$\rho = (4/\pi)^{\eta} \text{ and } \eta = 1 + r_{\min} / r_{\max}.$$
 (2.18)

Here, r_{min} and r_{max} represent corresponding smaller and larger radii of the rectangular coils, respectively. The value of ρ , evaluated from (2.18), is used in (2.17) to estimate M between rectangular planar coils.

For different lateral displacements, a_i and b_j are used to calculate parameters α , β , γ and δ , and M can be expressed as

$$M = \rho \times \sum_{i=1}^{i=n_p} \sum_{j=1}^{j=n_s} M_{ij}$$
 and

$$M_{ij} = \frac{\mu_0 \pi \, a_i^2 b_j^2}{2(a_i^2 + b_i^2 + z^2 + x^2)^{3/2}} \left[1 - \frac{3}{2} \delta_{ij} + \frac{15}{32} \gamma_{ij}^2 \left(1 - \frac{21}{2} \delta_{ij} \right) + \frac{15}{16} \left(\alpha_{ij}^2 + \beta_{ij}^2 \right) \left(1 - \frac{7}{4} \delta_{ij} \right) \right], \quad (2.19)$$

where
$$\delta_{ij} = x^2/(a_i^2 + b_j^2 + z^2 + x^2)$$
, $\gamma_{ij} = 2a_ib_j/(a_i^2 + b_j^2 + z^2 + x^2)$, $\alpha_{ij} = 2xa_i/(a_i^2 + b_j^2 + z^2 + x^2)$ and $\beta_{ij} = 2xb_j/(a_i^2 + b_j^2 + z^2 + x^2)$.

2.3.2 Comparison with 3D EM simulation

To compare the proposed model with the numerical solution, 3D EM simulations of different wireless power links were done in HFSS v.11 [8]. The turn number for both the primary and secondary coils was one ($n_S = n_P = 1$), the track width was 50 µm ($w_p = w_s = 50$ µm), the track separation was 20 µm ($s_p = s_s = 20$ µm), and the track thickness was 10 µm. During the 3D EM simulation, the resistivity of the copper tracks was set to 2.0 µ Ω • cm. In the first set of simulations, three different secondary coil radii ($r_{out_s} = 3$, 4 and 5 mm) were considered, while the primary coil radius was 10 mm ($r_{out_p} = 10$ mm) and the coil shape was circular. 3D EM simulation was done using the specified parameters, and the obtained M is presented in Fig. 2.5(a). Low frequency M was computed at 5 MHz during simulation as the self-resonance frequency of all the primary and secondary coils is at GHz range. And to predict M analytically,

(2.17) was employed using the above mentioned parameters. Fig. 2.5(b) shows the comparison between the predicted and 3D EM simulation results. Here, the axial distance was normalized to the maximum radius of the coils (in these cases, maximum radius, $r_{max} = r_{out_p} = 10$ mm) to visualize the applicable area of the model. Fig. 2.5(b) shows that the error decreases at larger axial distances. Even though the model shows the worst case scenario at a normalized distance of 0.01, the model can easily predict M, and the error is only about 6%. According to the wireless charging standard [20], to achieve higher efficiency ($\geq 90\%$) in wireless power applications, the ratio between the axial distance and the diameter of the coil should be less than or equal to 0.1, i.e., $z/(2 \times r_{max}) \leq 0.1$. Our model can suitably predict M for such a small axial separation, even at $z/(2 \times r_{max})$ equal to 0.005 (which is much less than 0.1).

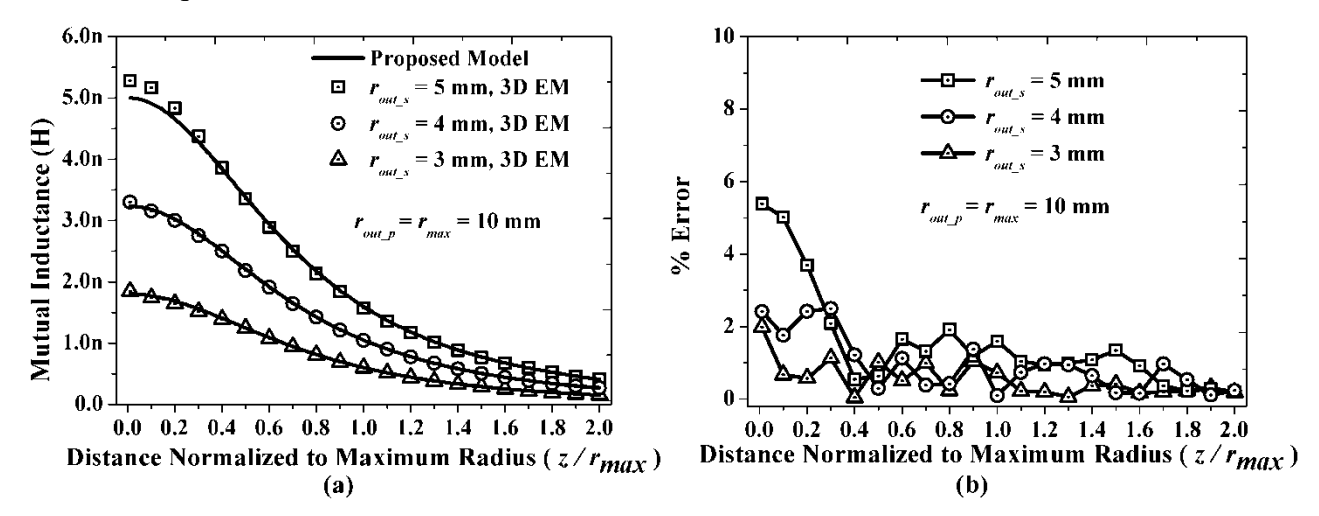


Figure 2.5: (a) *M* at different separation distances using 3D EM simulation results and the proposed model. (b) Comparison between the proposed model and the 3D EM simulation results in terms of error.

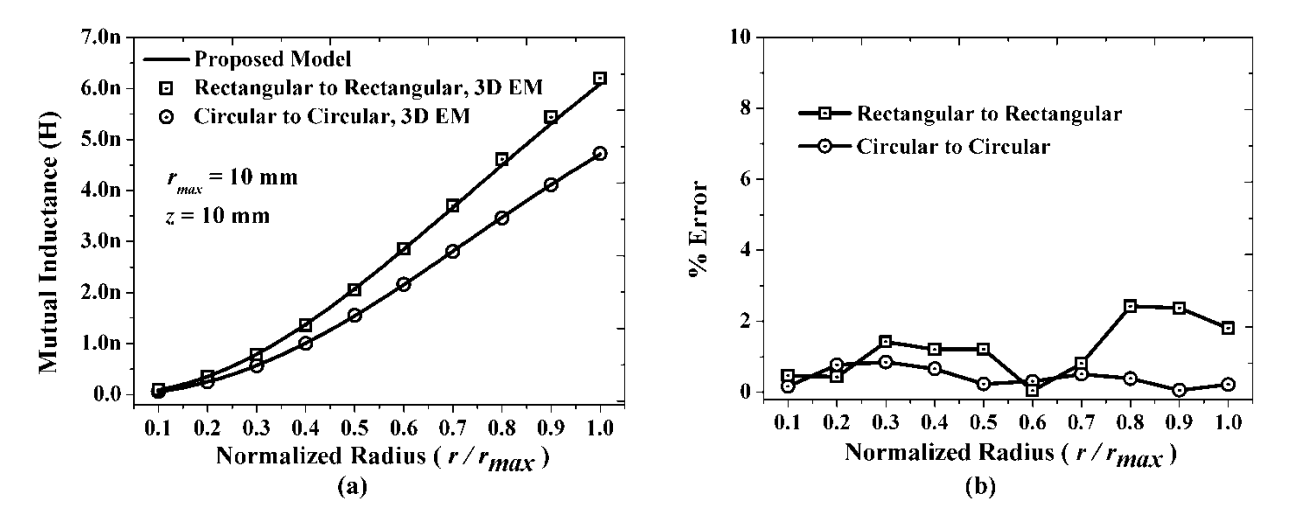


Figure 2.6: (a) Variation of M with different coil radii and coil shapes, and (b) comparison with the numerical results.

Another investigation was done for different coil radii by comparing the model with the 3D EM simulation result in Fig. 2.6(a). Here, the primary coil radius was fixed at 10 mm, the secondary coil radius was changed from 1 mm to 10 mm (normalized coil radius 0.1 to 1), and the track width and separation were similar to the first investigation. The axial separation was fixed at 10 mm and the turn number for both the primary and secondary coil was *one*. Fig. 2.6(a) shows that the model can suitably predict M for the circular to circular coils. Equation (2.17) was used for the analytical prediction of M. To calculate M for the rectangular to rectangular coils, (2.18) was employed in the model. In this case, one side of the rectangular coil was equal to the diameter (2r) of the corresponding circular coil for different radii of the coils. Fig. 2.6(b) shows that the model can predict M for circular-to-circular coils and rectangular-to-rectangular coils of different radii, while incurring little error.

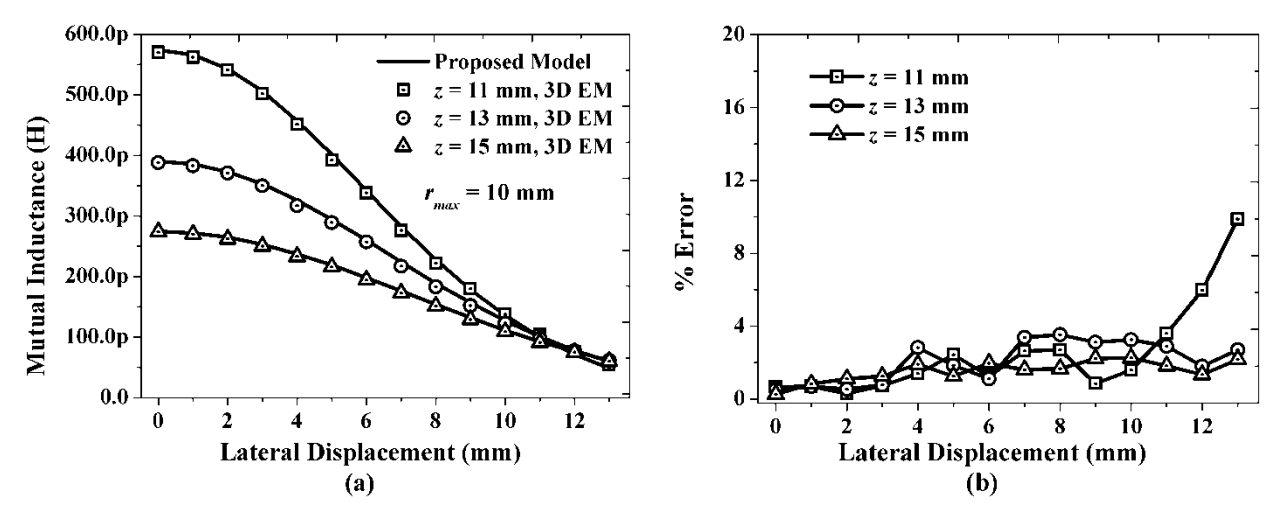


Figure 2.7: Variation of *M* at different lateral displacements, and (b) comparison with a 3D EM simulation results.

The variation of M due to lateral displacement was also investigated using 3D EM simulations. In this set of simulations, both the primary and secondary coil radii were 10 mm, track width and separation were similar to the first investigation, and the shape was circular. Equation (2.19) was employed to predict M analytically. The lateral displacements at different axial separation

distances are shown in Fig. 2.7(a). Fig. 2.7(b) shows that the model can suitably predict M for different lateral displacements, while allowing small error. However, for a smaller axial separation (in this case, z = 11 mm), if the lateral displacement is higher than the maximum radius of the coil ($x > r_{max}$), the error becomes larger. But in such a large lateral displacement, M approaches towards zero, and high accuracy of the model may not be required in practice. For the lateral displacement, the working region of the model is outlined as $x < r_{max}$.

2.3.3 Experimental verification of the mutual inductance model

To validate the proposed model experimentally, two types of wireless power links were constructed using fabricated planar coils: PCB to PCB wireless power links and PCB to on-chip wireless power links. In the first set of measurements, M between a planar PCB and PCB coils was measured. The geometric parameters of these setups are described in Table 2.2 and categorized as Link-1 and Link-2. Both inductors in Link-1 were rectangular shaped, while in Link-2, both of them were circular. The electrical measurement setup for Link-1 and Link-2 is shown in Fig. 2.8(a). Links-1 and 2 are sample examples of the setup for applications like contactless battery charging platforms [21-23], [24] and biomedical implants [25], [26], where the coil size is large.

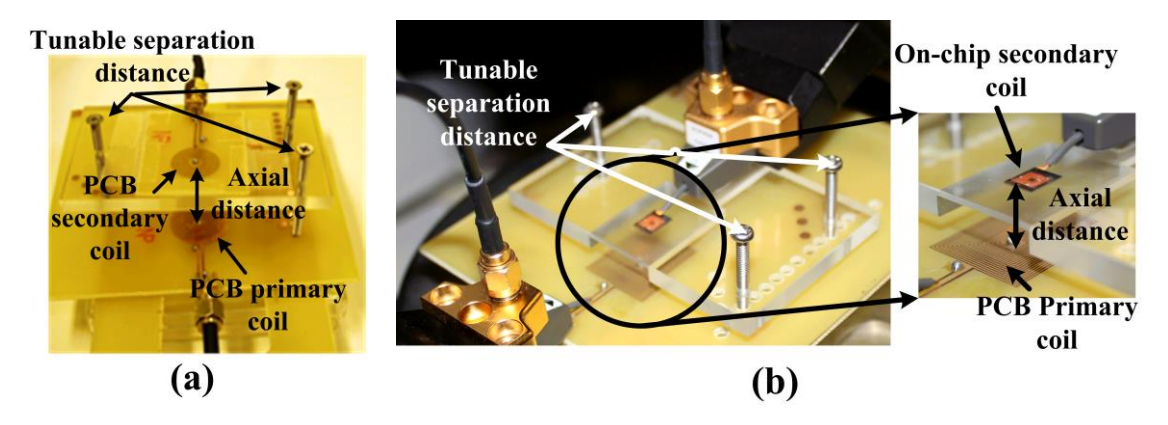


Figure 2.8: Measurement setup for (a) PCB and PCB coils, (b) PCB and on-chip coil.

To measure the low frequency M (@ 1 MHz), 2-port s-parameter measurements were performed using an R&S ZVB8 vector network analyzer (VNA). One port of the VNA was connected to the primary coil and another to the secondary coil. The VNA has a signal generator whose frequency and amplitude can be varied. During the measurement process, a signal with a specific frequency

and amplitude passed through the device under test (DUT) using one of the ports, while another port was terminated by a 50 Ω load. Both the phase and amplitude of the reflected and transmitted signals were detected by the VNA. From this information the VNA generated sparameters for one of the ports. As an example, when the test signal was passed through port-1, it generated S_{11} and S_{21} . The VNA did a similar routine for all ports and generated S_{11} , S_{21} , S_{22} and S_{12} . These 2-port s-parameters were converted to Z-parameters (Z_{11} , Z_{12} , Z_{21} , and Z_{22}). At a specific frequency f, M was calculated as $Im(Z_{12})/2\pi f$ or $Im(Z_{21})/2\pi f$.

TABLE 2.2

GEOMETRIC PARAMETERS OF WIRELESS POWER LINKS CONSTRUCTED BY DIFFERENT TYPES OF PLANAR INDUCTORS

Coil Geometric	PCB to PCB Wireless Power Links		PCB to On-Chip Wireless Power Links		
Parameters	Link-1	Link-2	Link-3	Link-4	Link-5
r _{out_p}	10 mm	10 mm	10 mm	10 mm	10 mm
r_{out_s}	7.5 mm	7.5 mm	2.25 mm	2.25 mm	1.25 mm
n_P	17	17	17	17	17
n_S	11	11	37	37	21
w_p	250 μm	250 μm	250 μm	250 μm	250 μm
w_s	250 μm	250 μm	30 μm	30 μm	30 μm
S_p	250 μm	250 μm	250 μm	250 μm	250 μm
S_S	250 μm	250 μm	15 µm	15 μm	15 μm
Coil shape	Both Rec	Both Cir	Both Rec	Both Cir	Both Rec

Rec: Rectangular, Cir: Circular

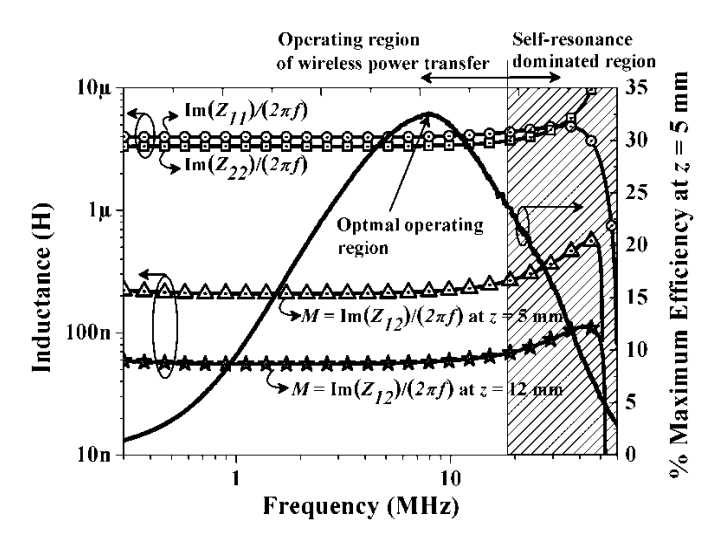


Figure 2.9: Experimental extraction of inductances and maximum achievable efficiency for Link-3 at different operating frequencies.

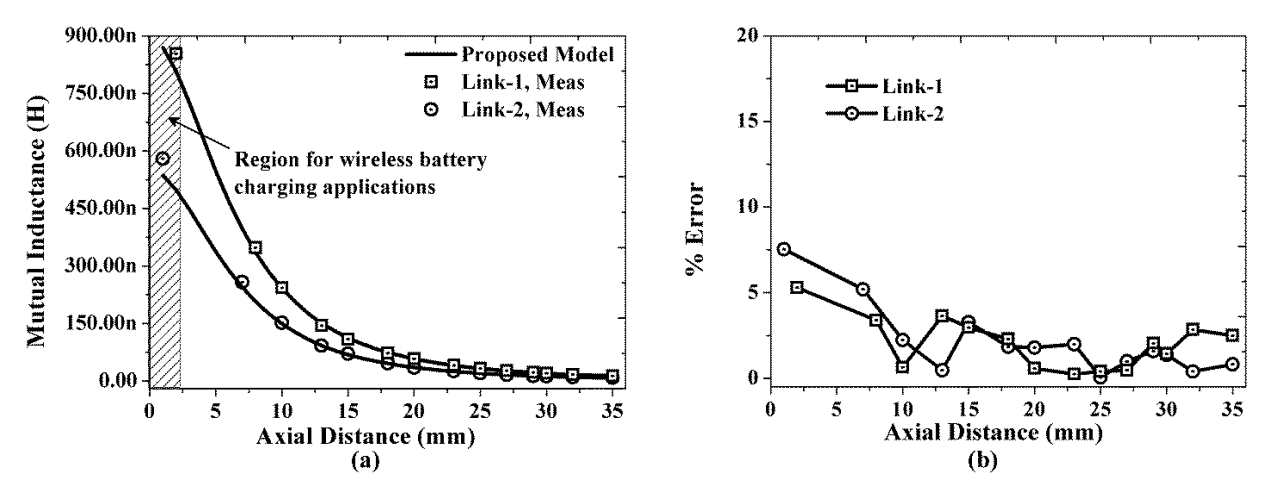


Figure 2.10: (a) Measured values of M at different axial separations between a planar PCB and PCB coils (Links-1 & 2); and (b) comparison with the predicted results in terms of error.

There is a dependency of M with respect to frequency that was observed during the 3D EM simulation and measurement results as well. Parasitic effects are the primary source of frequency dependency which includes mutual capacitance between two coils and an increase in resistance due to the eddy current generated by the proximity effect. The frequency dependency only starts having an effect near the self-resonance frequency of the inductor. For higher power transfer efficiency, the operating frequency should be maintained below the self-resonance dominated region. Thus, in the range of the operating frequency, M shows very little dependency on

frequency and can be modeled as low frequency values for practical purposes. As an example, experimental extraction of inductances for Link-3 at different operating frequencies is shown in Fig. 2.9. Experimental data confirms that the maximum achievable efficiency starts to roll off in the self- resonance dominated region, as presented in Fig. 2.9. This is because, in the self-resonance dominated region, the inductor quality factor (Q) starts to degrade [27] and in turn causes lower power transfer efficiency [2]. Hence, the operating frequency for wireless power transfer should be below the self-resonance dominated region, as shown in Fig. 2.9. This confirms that the model can be used to predict M in the practical operating frequency range for wireless power transfer.

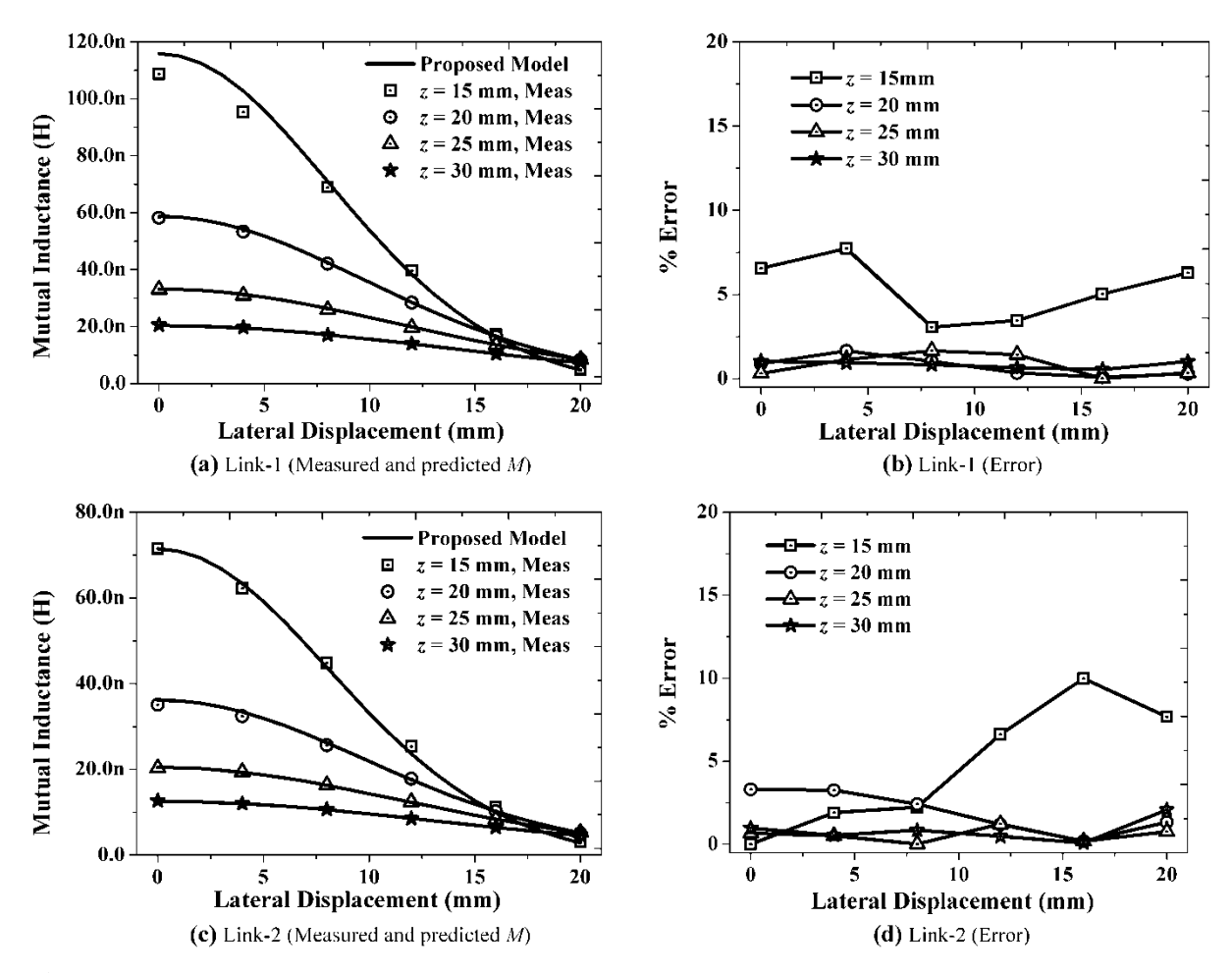


Figure 2.11: (a) Measured and predicted *M* due to lateral displacement at different axial distances for Link-1 (rectangular shaped PCB to PCB coils). (b) Comparison between measured and predicted results for Link-1. (c) Measured and predicted *M* due to lateral displacement for Link-2 (circular shaped PCB to PCB coils). (d) Comparison between measured and predicted

results.

Fig. 2.10(a) shows the measurement results for both Links-1 and 2 at different axial separations. To calculate M for both of these links, (2.17) was employed using the parameters specified in Table 2.2. A comparison between the measured and predicted results is also presented in Fig. 10(b). In wireless charging applications, the diameters ratio of the secondary and primary coils should about $0.5\sim1$ [45], and to achieve higher efficiency, the coils should be placed as closely as possible, i.e., $z/(2\times r_{out_p})\approx 0.1$, as mentioned in Section 2.3.2. Links-1 and 2 are examples of such systems. Here, the diameter ratio is (7.5mm/10mm) 0.75. Measurements were done for Links-1 and 2 for axial distances as close as about 2 mm, as shown in Fig. 10(a). At 2 mm axial distance, $z/(2\times r_{out_p})$ is equal to 0.1, and the analytical model can predict M ,incurring little error (< 10%). Thus, this model can be used in wireless battery charging platforms.

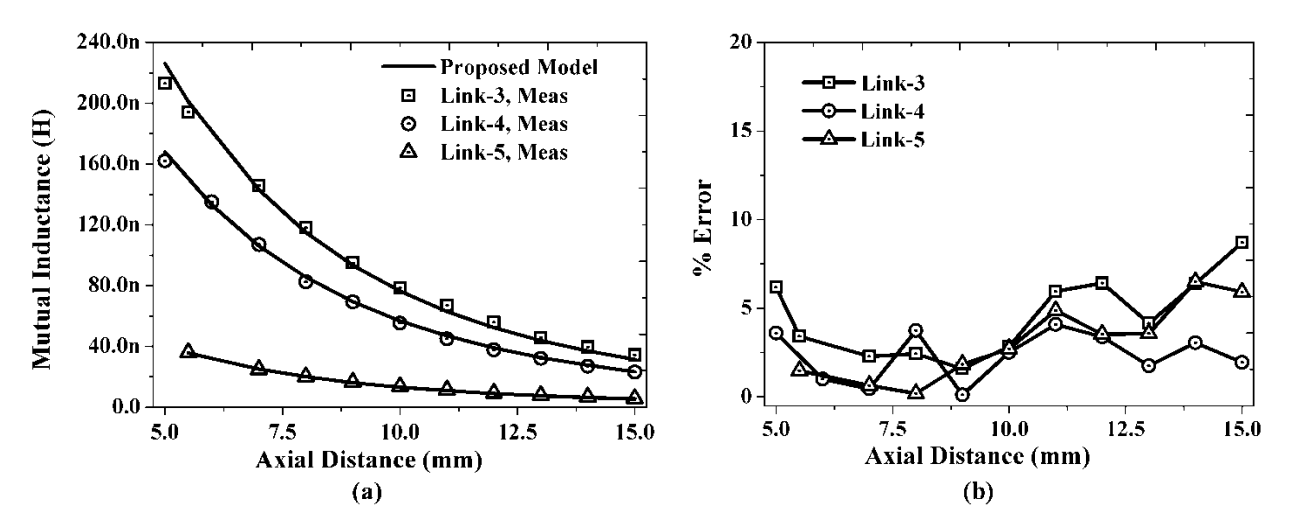


Figure 2.12: (a) Measured values of M at different axial separations between a planar PCB and on-chip coils (Links-3, 4 & 5); and (b) comparison with the predicted results.

Again, M at different axial and lateral displacements was measured for both Links-1 and 2, and the results are shown in Fig. 2.11. Equation (2.19) was used to predict M for the lateral displacement. Calculated results for both Link-1 and Link-2 are compared with the measurement results, and the error is limited to 10%.

Emerging applications like transcutaneous wireless power transfer systems have a small receiving coil size compared to the transmitting coil [28] and are fabricated on silicon [29], [30]. To verify the model for these kinds of systems, Link-3, Link-4 and Link-5 were constructed as described in Table 2.2. The measurement setup for Link-3, Link-4 and Link-5 is shown in Fig. 2.8(b). Different coil shapes were also considered in these cases.

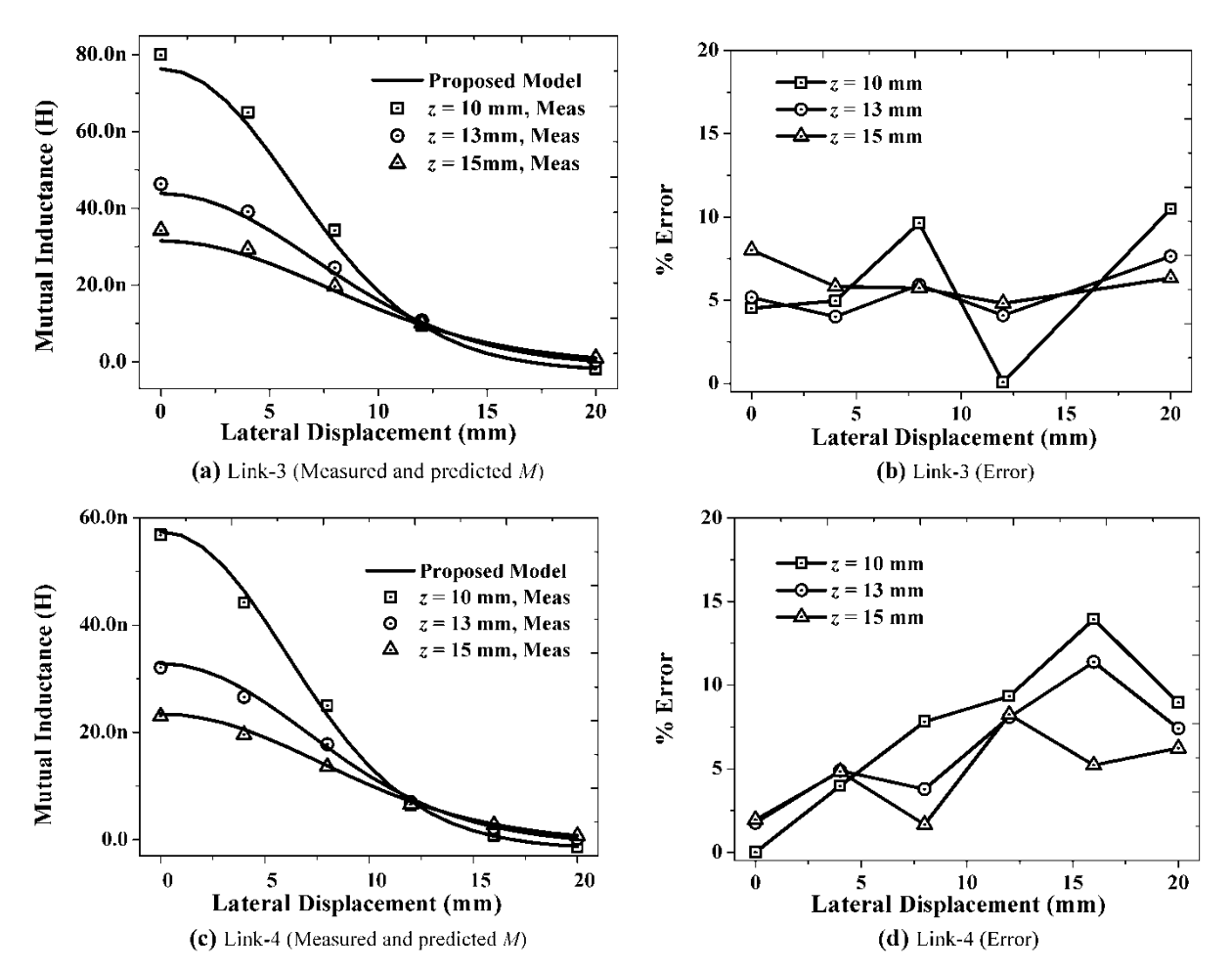


Figure 2.13: (a) Measured and predicted *M* due to lateral displacement at different axial distances for Link-3 (rectangular shaped PCB to rectangular shaped on-chip coils). (b) Comparison between measured and predicted results for Link-3. (c) Measured and predicted *M* due to lateral displacement for Link-4 (circular shaped PCB to circular shaped on-chip coils), and (d) comparison between measured and predicted results.

Intrinsically, the axial distance between the primary and secondary coils is quite large for medical implant devices. For example, brain implant applications require an inter-coil distance of at least 5 mm (scalp thickness [31]) or 12 mm (scalp thickness + skull thickness [32]) and cardiac implants require a much higher axial distance of about 5 cm [33]. This is why this set of measurements was done at higher axial distances. Fig. 2.12(a) shows the measured M for Links-3, 4 & 5 at different axial separations. Here, the prediction was done using (2.17) for all of these links, using the parameters described in Table 2.2. And the comparison in Fig. 2.12(b) shows that the error is limited to 10% in these cases. As the coil radius is very small for the rectangular coils described in Links-3 and 5, the average value of parameter η , equal to 1.225 and 1.125 respectively, is considered in each respective case during the calculation.

In Fig. 2.13, calculated M at different axial and lateral displacements is compared with the measurement results for both Links-3 and 4, and the maximum error is limited to 15%. The error that occurred during this measurement setup was large compared to the previous one. However, as the coil radius was very small in these cases, small imprecision control could have led to a large measurement error.

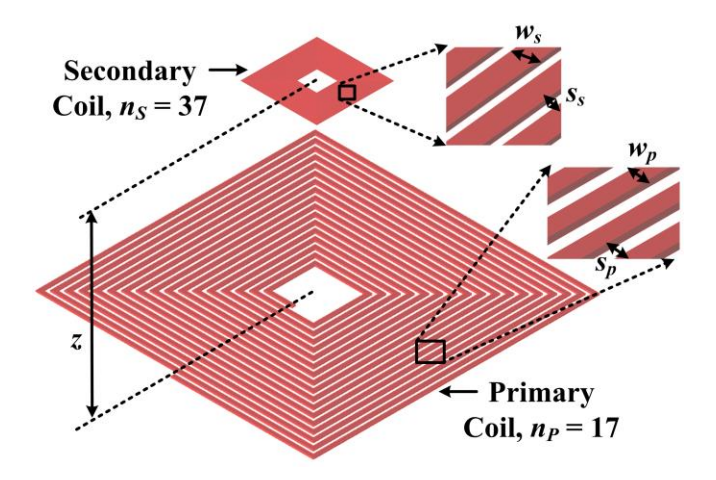


Figure 2.14: 3D simulation system of Link-3 in HFSS.

2.3.4 Computational efficiency and future extension

The effectiveness of the model is investigated by comparing the simulation time of the 3D numerical method and proposed analytical model. The sample simulation times for the different wireless links are described in Table 2.3. The simulation was done using an Intel(R) Core(TM) i7 CPU with processor speed of 2.93 GHz and 16.0 GB of RAM. Solving any system in a 3D EM simulator requires a lot of computational efficiency. Here, Link-3 is used as a simulation

example. At the beginning of the EM simulation, the 3D geometry of Link-3 was drawn in HFSS, as shown in Fig. 2.14. To obtain the 2-port s-parameter, both the primary and secondary coils were excited using lumped ports. In HFSS, the lumped port worked as a signal source with a user defined impedance of 50Ω . During simulation, the geometric model was automatically divided into a large number of tetrahedra. By representing the value of the field quantity for each tetrahedron, the system transformed Maxwell's equations into matrix equations. Then the Maxwell's equations were solved numerically [35]. After the solution, both the transmitted and reflected signals from each port were calculated to obtain the 2-port s-parameter. During the simulation, about 400×10^3 tetrahedra were created. Solving the Maxwell's equations for this large number of elements led to extensive use of computational efficiency and time. This is why the simulation of Link-3 using the 3D EM method required more than two hours (about 7572 s), whereas the proposed model required merely 14×10^{-3} sec. The simulation time was also evaluated for another numerical approach using the numerical integration of complete elliptic functions [40], and it was about 2.073 sec. These data confirm that a lot of simulation time can be saved (10⁶ orders compared to 3D EM, and 1.5×10² orders compared to [40]) using the proposed model and, most importantly, complex numerical simulations can be avoided.

TABLE 2.3

COMPARISON OF SIMULATION EFFICIENCY

Coil Specifications	Required Simulation	Simulation Method
	Time	
$n_P = 1$, $n_S = 1$ (Any two coil system	3 min 13 sec	3-D EM, HFSS
described in Section 2.3.2)		
$n_P = 17, n_S = 21 \text{ (Link-5)}$	37 min 14 sec	3-D EM, HFSS
$n_P = 17, n_S = 37 \text{ (Link-3)}$	2 hr 6 min 12 sec	3-D EM, HFSS
$n_P = 17, n_S = 37 \text{ (Link-3)}$	2.073 sec	Using numerical integration of
		complete elliptic functions [40]
$n_P = 17, n_S = 37 \text{ (Link-3)}$	$14 \times 10^{-3} \text{ sec}$	Proposed Model

In some power transfer applications, researchers use a ferromagnetic core to increase M [34] between inductors. Inserting ferromagnetic material within the coils increases the magnetic flux generated inside the space enclosed by the coil and thus increases M. The increment factor

depends on the relative permeability (μ_r) and the shape of the ferromagnetic core [34]. The proposed model can be readily extended for this case by inserting a scaling factor for μ_r into the equation for computing M.

2.5 Wireless power link efficiency and voltage gain

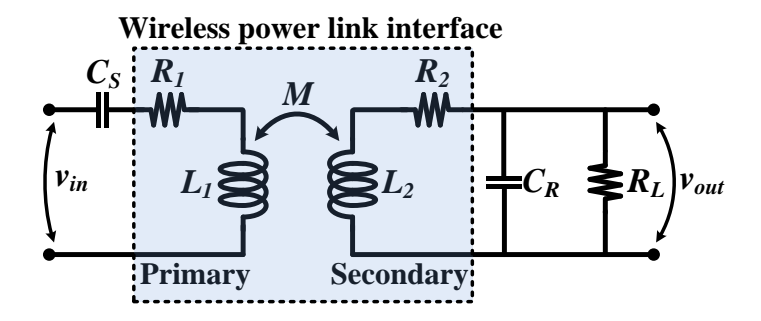


Figure 2.15: Simplified schematic diagram of a wireless power link with lumped equivalent circuit elements.

A simplified schematic model of an inductive power link is presented in Fig. 2.15. The electrical parameters (L_1 , R_1 , L_2 , R_2 and M) of an inductive power link can be calculated using (2.1) – (2.19). To achieve the highest voltage gain and maximum power frequency, two external capacitances, C_S and C_R , are added (as shown in Fig. 2.15) to resonate the primary and secondary sides with each other. At a specific frequency f, C_S and C_R can be determined as

$$C_S = \frac{1}{4\pi^2 f^2 L_1}$$
, and $C_R = \frac{1}{4\pi^2 f^2 L_2}$.

The coupling coefficient *k* is the key parameter to calculate the power transfer efficiency, which is defined as the ratio between the mutual and self inductances and is expressed as

$$k = \frac{M}{\sqrt{L_1 L_2}}.$$

In practical applications, the inductive power link has to drive some electrical loads like the rectifier and voltage regulator. For now, these loads are represented by the load resistance R_L , as

shown in Fig. 2.15. To calculate the power efficiency and voltage gain, let us introduce parameter X and the load factor α , which are expressed as

$$X = k^2 Q_1 Q_2, \text{ and } \alpha_L = \omega C_R R_L. \tag{2.20}$$

Here, Q_1 ($\omega L_1/R_1$) and Q_2 ($\omega L_2/R_2$) are the quality factors of the primary and secondary inductors, respectively. According to [35], the inductive link's power efficiency (η_{link}) at different loads can be calculated as

$$\eta_{link} = \frac{X Q_2}{\left(\alpha_L + Q_2\right) \left(\frac{Q_2}{\alpha_L} + X + 1\right)}.$$
(2.21)

Maximum achievable link efficiency (η_{max}) can be determined as

$$\eta_{\text{max}} = \frac{X}{\left(1 + \sqrt{1 + X}\right)^2} \,.$$
(2.22)

And the voltage gain (A_V) at different loaded conditions can be described as

$$A_{V} = \frac{v_{out}}{v_{in}} = \frac{\omega M Q_{2}}{R_{1}} \sqrt{\frac{1 + \alpha_{L}^{2}}{(\alpha_{L} + Q_{2} + \alpha_{L} X)^{2} + Q_{1}^{2}(\alpha_{L} + Q_{2})^{2}}}.$$
 (2.23)

2.6 Characterization of wireless power link and model verification

To validate the proposed model experimentally, an inductive power link was implemented using planar inductors. The geometric parameters of the implemented inductive Link-1 are described in Table 2.2. 2-port s-parameter measurements were performed using an R&S ZVB8 vector network analyzer (VNA). These 2-port s-parameters were converted to Z-parameters (Z_{11} , Z_{12} , Z_{21} , and Z_{22}). At a specific frequency, L_1 , R_1 , L_2 , R_2 and R_3 was evaluated as $Im(Z_{11})$, $Im(Z_{22})$, $Im(Z_{22})$ and $Im(Z_{12})/2\pi f$, respectively. Then, a similar set of measurements were performed at various axial separations and lateral displacements. In these cases, L_1 , R_1 , L_2 , and R_2 remained unchanged, but R_3 was changed drastically with its relative placement and in the analytical model, this effect is captured by (2.19). Equation (2.22) was adopted to calculate the maximum achievable efficiency at different axial and lateral displacements.

Fig. 2.16 shows the maximum achievable efficiency by the implemented inductive link at various operating frequencies. Measurements were done for both 10 mm and 15 mm axial

separations between the primary and secondary inductors. In both of the cases, the proposed model can suitably predict the maximum efficiency in the entire range of frequency. The model can also clearly identify the operating frequency at which η_{max} reaches its peak.

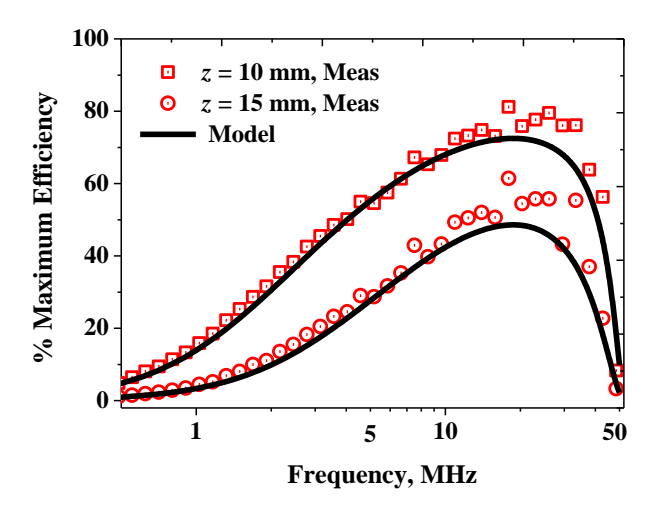


Figure 2.16: Maximum achievable efficiency at different operating frequencies. Measurement was done both at 10 mm and 15 mm axial separations between the primary and secondary inductors.

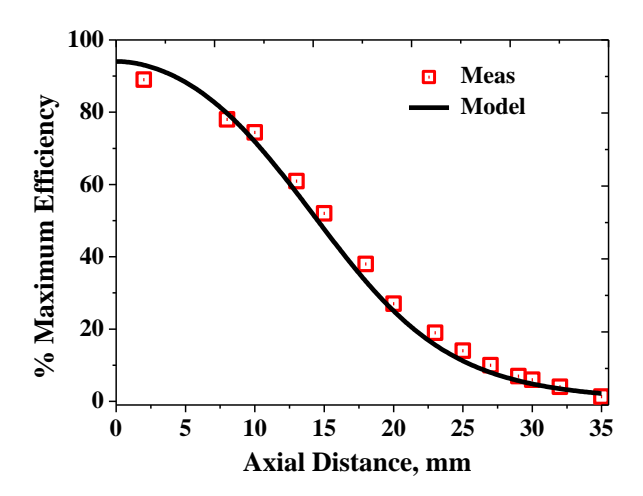


Figure 2.17: Maximum achievable efficiency at different axial separations, while operating frequency was fixed at 13.56 MHz.

Fig. 2.17 compares η_{max} at different axial separations, while the operating frequency was fixed at 13.56 MHz. In Fig. 2.18, η_{max} is also compared for different lateral displacements at similar operating frequencies. In both of these cases, the calculated and measured results are in agreement.

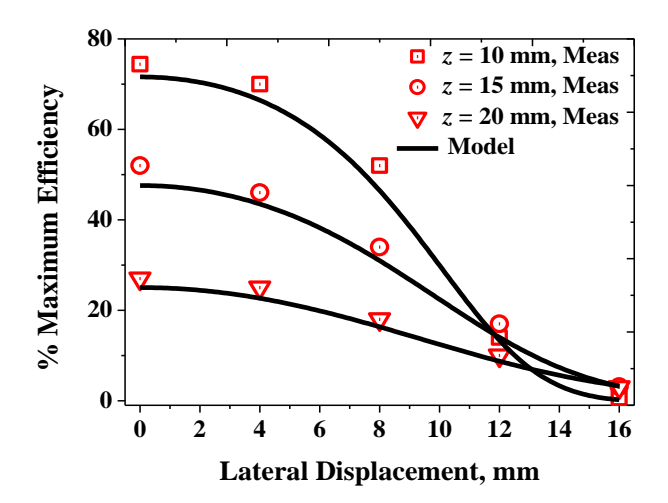


Figure 2.18: Variation of maximum achievable efficiency due to different lateral displacements, while operating frequency was at 13.56 MHz.

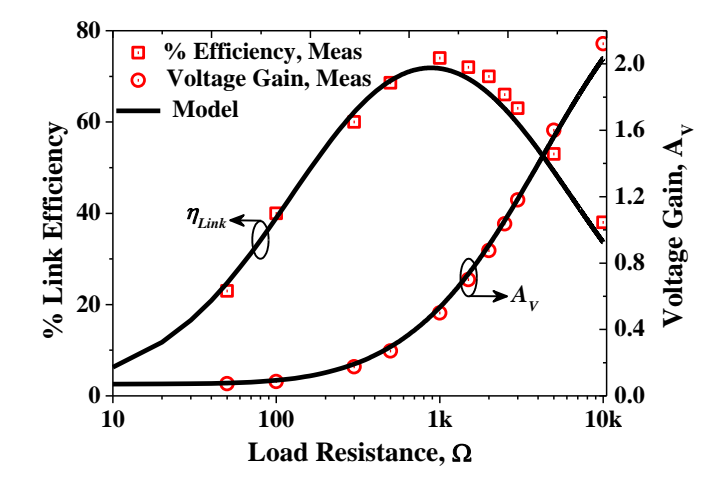


Figure 2.19: Measured efficiency and voltage gain at different load resistances. In this set of measurements, the frequency was at 13.56 MHz and the relative axial distance between inductors fixed at 10 mm.

Also, another set of measurements was performed to capture the effect of the load resistance on the link efficiency. In these measurements, the operating frequency was at 13.56 MHz and the axial separation was fixed at 10 mm; however, the load resistance was varied from 50 Ω to 10 K Ω . To drive the primary and secondary inductors in resonance at 13.56 MHz, the external capacitor C_S was set at 40 pF and C_R was at 100 pF. Fig. 2.19 shows the measured η_{link} and A_V at different load resistances. In this case, (2.21) and (2.23) were adopted to calculate η_{link} and A_V respectively. Again, the proposed model captures the measurement results in a satisfactory manner. Fig. 2.19 shows that η_{link} reaches towards η_{max} at a load resistance of 1 K Ω ; thus this model can also can predict the load at which η_{link} maximizes.

Through measurement results, it was observed that the link efficiency and voltage gain of an inductive power link are affected by the geometric parameters of the system. Designers also need to know the optimal operating frequency and load at which the power link efficiency maximizes. As the model can easily capture all of these critical design parameters, the effectiveness of this prediction technique is confirmed.

References

- [1] A. Ramrakhyani, S. Mirabbasi and M. Chiao, "Design and optimization of resonance-based efficient wireless power delivery systems for biomedical implants," *IEEE Transactions on Biomedical Circuits and Systems*, vol. 5, no. 1, pp. 48-63, Feb. 2011.
- [2] U.-M. Jow and M. Ghovanloo, "Design and optimization of printed spiral coils for efficient transcutaneous inductive power transmission," *IEEE Transactions on Biomedical Circuits and Systems*, vol. 1, no. 3, pp. 193-202, Sep 2007.
- [3] R.R. Harrison, "Designing efficient inductive power links for implantable devices," *IEEE International Symposium on Circuits and Systems*, New Orleans, pp. 2080-2083, USA, May 2007.
- [4] R. Jegadeesan, and Y.-X. Guo, "Topology selection and efficiency improvement of inductive power links," *IEEE Transactions on Antennas and Propagation*, vol. 60, no.10, pp. 4846–4854, Oct. 2012.
- [5] A. P. Sample, D. A. Meyer, J. R. Smith, "Analysis, experimental results, and range adaptation of magnetically coupled resonators for wireless power transfer," *IEEE Transactions on Industrial Electronics*, vol. 58, no. 2, pp. 544-554, Feb. 2011.

- [6] X. Zhang, S. L. Ho, and W. N. Fu, "Quantitative analysis of a wireless power transfer cell with planar spiral structures," *IEEE Transactions on Magnetics*, vol. 47, no.10, pp. 3200–3203, Oct. 2011.
- [7] X. Liu, W.M. Ng, C.K. Lee, and S.Y. Hui, "Optimal operation of contactless transformers with resonance in secondary circuits," *Applied Power Electronics Conference and Exposition*, pp. 645–650, Feb. 2008.
- [8] HFSS v.11, ANSYS, Inc., Canonsburg, USA, 2007.
- [9] S. S. Mohan, M. M. Hershenson, S. P. Boyd, and T.H. Lee, "Simple accurate expressions for planar spiral inductors", *IEEE Journal of Solid-State Circuits*, Vol. 34, No. 10, pp. 1419-1424, October 1999.
- [10] W. B. Kuhn and N. M. Ibrahim, "Analysis of current crowding effects in multiturn spiral inductors", *IEEE Trans. Microw. Theory Tech.*, vol. 49, no. 1, pp.31 -38 200.
- [11] F. W. Grover, "Inductance Calculation: Working Formulas and Tables," *New York: Dover Publications*, 1946.
- [12] M. Soma, D. C. Galbraith and R. L. White, "Radio-frequency coils in implantable devices: Misalignment analysis and design procedure," *IEEE Transaction on Biomedical Engineering*, vol. BME-34, no.4 pp.276-282, April 1987.
- [13] K.B. Kim, E. Levi, Z. Zabar, and L. Birenbaum, "Mutual inductance of noncoaxial circular coils with constant current density," *IEEE Transaction on Magnetics*, vol. 33, no.5, pp. 4303-4309, Sept. 1997.
- [14] S. Babic, et. al., "New formulas for mutual inductance and axial magnetic force between a thin wall solenoid and a thick circular coil of rectangular cross-section," *IEEE Transactions on Magnetics*, vol: 47, no: 8, pp. 2034-2044, Aug. 2011.
- [15] S. I. Babic, F. Sirois, C. Akyel and C. Girardi "Mutual inductance calculation between circular filaments arbitrarily positioned in space: Alternative to Grover's formulas," *IEEE Transaction on Magnetics*, vol. 46, no. 9, pp.3591-3600, Sept. 2010.
- [16] W. G. Hurley and M. C. Duffy, "Calculation of self and mutual impedances in planar magnetic structures," *IEEE Transactions on Magnetics*, vol.31, no.4, pp.2416-2422, July 1995.

- [17] C.M Zierhofer, E.S. Hochmair, "Geometric approach for coupling enhancement of magnetically coupled coils," *IEEE Transactions on Biomedical Engineering*, vol. 43, no.7, pp. 708-714, July 1996.
- [18] J T. Conway, "Inductance calculations for noncoaxial coils using Bessel functions," *IEEE Transactions on Magnetics*, vol.43, no.3, pp. 1023-1034, March 2007.
- [19] C.L.W. Sonntag, E.A. Lomonova, and J.L. Duarte, "Implementation of the Neumann formula for calculating the mutual inductance between Planar PCB inductors," *International Conference on Electrical Machines*, Vilamoura, Portugal, Sept. 2008.
- [20] "Technical notes of Wireless Power Consortium," 2012. [Online]. Available: http://www.wirelesspowerconsortium.com/technology/transfer-efficiency.html
- [21] X. Liu and S. Hui, "Optimal design of a hybrid winding structure for planar contactless battery charging platform," *IEEE Transaction on Power Electronics*, vol.23, no.1, pp. 455-463, Jan 2008.
- [22] E. Waffenschmidt, "Wireless power for mobile devices," *IEEE International Telecomunications Energy Conference*, Amsterdam, Oct. 2011.
- [23] H. Marques, and B. Borges, "Contactless battery charger with high relative separation distance and improved efficiency," *International Telecommunications Energy Conference*, Oct. 2011.
- [24] B. Choi, J. Nho, H. Cha, T. Ahn, and S. Choi, "Design and implementation of low-profile contactless battery charger using planar printed circuit board windings as energy transfer device," *IEEE Transaction on Industrial Electronics*, vol. 51, no. 1, pp. 140-147, Feb. 2004.
- [25] S. O'Driscoll, A. Poon and T. Meng "A mm-sized implantable power receiver with adaptive link compensation", *IEEE International Solid-State Circuits Conf. Dig. Tech. Papers*, pp.294-295, 2009.
- [26] C. Koch, W. Mokwa, M. Goertz, and P. Walter, "First results of a study on a completely implanted retinal prosthesis in blind humans," *IEEE Sensors Conference*, pp. 1237-1240, Oct. 2008.
- [27] C. P. Yue, S. S. Wong, "Physical modeling of spiral inductors on silicon," *IEEE Transaction of Electron Devices*, Vol. 47, No.3, pp. 560-568, March 2000.

- [28] R. Wu, S. Raju, M. Chan, J. K.O. Sin and C. P. Yue, "Wireless power link design using silicon-embedded inductors for brain-machine interface," *International Symposium on VLSI Design, Automation and Test*, Hsinchu, Taiwan, April 2012.
- [29] R. Wu, S. Raju, M. Chan, J. K.O. Sin and C. P. Yue, "Silicon-embedded coil for high-efficiency wireless power transfer to implantable biomedical ICs," *IEEE Electron Device Letters*, vol. 34, no. 1, pp. 09-11, Jan. 2013.
- [30] R.R. Harrison *et al.*, "A low-power integrated circuit for a wireless 100-electrode neural recording system," *IEEE Journal of Solid-State Circuits*, vol. 42, no. 1, pp. 123-133, Jan. 2007.
- [31] H. Hori et al., "The thickness of human scalp: normal and bald," *Journal of Investigative Dermatology*, vol. 58, no. 6, pp. 396-399, 1972.
- [32] "Study: women's skulls thicker, men's wider; might affect protection design," Occupational Health & Safety, January 2008
- [33] S. Kim, J. S. Ho, L. Y. Chen, and A. S. Y. Poon, "Wireless power transfer to a cardiac implant," *Applied Physics Letters*, vol. 101, p. 073701, August 2012.
- [34] P.T. Theilmann and P.M. Asbeck, "An analytical model for inductively coupled implantable biomedical devices with ferrite rods," *IEEE Transactions on Biomedical Circuits and Systems*, vol. 3, no. 1, pp. 43-52, Feb. 2009.
- [35] B. Lenaerts, and R. Puers, *Omnidirectional inductive powering for biomedical implants*, Springer, 2009, pp. 39-54.

Chapter 3

Integrated wireless powering interface for sub-mm² size SoC

3.1 Design considerations of an integrated wireless power link

Wireless power links are a popular technique for short distance power transmission. A wireless power link is composed of two inductors that are magnetically coupled. The power efficiency depends on the operating frequency, the inductance, and the quality factor of the transmitting and receiving inductors and the coupling factor [1], [2] between them. For bio-applications, typically, the coupling factor is poor since the size of the implanted receiving inductor is limited due to its sub-mm² size (e.g., 5×5 mm² for a neural implant chip [3]) and the separation distance is relatively large (e.g., 5 mm [4] for neural implants just beneath the scalp to 12 mm [4], [5] for deep brain implants). The key challenge in maximizing the power efficiency is how to implement an implanted receiving coil with a large inductance and a high quality factor under the size constraint.

A number of wireless power links have been reported for implantable biomedical applications [6-12]. Most of them used wire-wound or printed-circuit-board (PCB) technologies to implement planar receiving coils [6-9]. The large line width and spacing provided by these technologies results in a limited number of turns and, therefore, a small receiving coil inductance density. Several wireless power link prototypes used IC fabrication technologies [10], [11] to attain a large receiving coil with high inductance [11]. However, the limited metal thickness (~5 μm) resulted in large series resistance and therefore a low quality factor of 2–6 [11]. Using magnetic materials to increase the inductance and quality factor is a common practice for on-chip power inductors [12] and has also been tried for receiving coils [11], [13]. However, since no magnetic material can be applied in the large separation between the coils, the mutual inductance can hardly be improved and the coupling factor will drop accordingly, unless an impractically thick magnetic core is employed [13]. The only practical way to realize a monolithic integrated power receiving coil is to use more turns and large track cross sectional areas as there is a linear relationship between the coil area and mutual inductance. Therefore, a new integration technique is required to implement a power receiving inductor which possesses the whole chip area. In this

chapter, we propose a practical way to create an on-chip power receiving inductor that can possess the whole chip area without affecting the on-chip active circuitry.

3.2 Silicon embedded inductor technology

Considering the above mentioned issues, in this work, a silicon embedded inductor [14] has been used to implement a power receiving coil for wireless power transfer to implanted biomicrosystems. In this technology, the inductor is fabricated in the thick bottom layer of the substrate and connected to the front end through vias. Thus, the whole chip area can be used to fabricate the power receiving coil.

3.2.1 Fabrication of the silicon embedded power receiving coil

Fig. 3.1 illustrates a schematic 3D view of a silicon-embedded power receiving coil. For the fabrication, a very thick (200 μm) high-aspect-ratio (7) Cu coil was integrated in the bottom layer of a silicon substrate. Only two vias were opened at the front-side of the substrate so that most of the front-side substrate area could still be used for active circuitry. Thus, the power receiving inductor area could be maximized to the implant size. These advantages rendered an extremely compact wireless powering interface for bio-implants since close to half of the silicon substrate volume was used to accommodate the power receiving coil. The micro-fabrication nature of the technology allowed many turns to be fabricated within the limited bio-implant size for a large mutual inductance (e.g. track width of 30 μm and separation of 15 μm). Still, due to its large metal thickness, a higher quality factor was obtained.

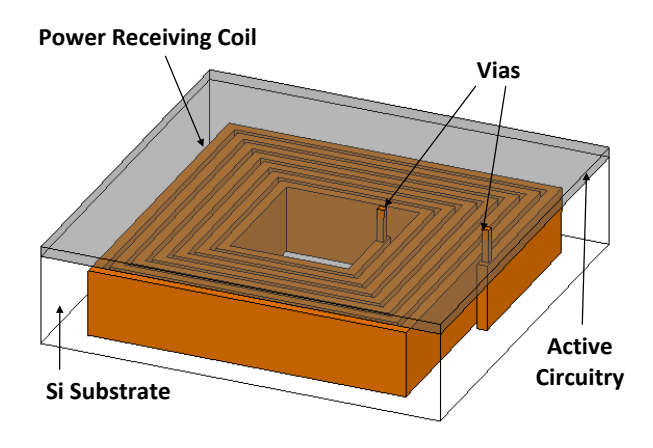


Figure 3.1: Schematic 3D illustration of a silicon embedded power receiving coil.

This technology is very similar to the front-side via-last through-silicon-via technology [17]; therefore, it can be easily integrated as a post-CMOS process. A layer of 1 μ m oxide was deposited to isolate the copper traces from directly contacting the silicon substrate. For normal substrate resistivity (10–30 Ω • cm) wafers, which are commonly used in a standard CMOS process, this oxide layer is essential in order to reduce the substrate loss. For this work, a high-substrate-resistivity (> 1000 Ω • cm) silicon wafer was adopted to reduce the substrate loss. Fig 3.2(a) shows the cross-sectional view of the embedded Cu tracks and vias, which was obtained from a test structure. Fig 3.2(b) shows the plane view of the fabricated embedded receiving coil from the back-side of the chip.

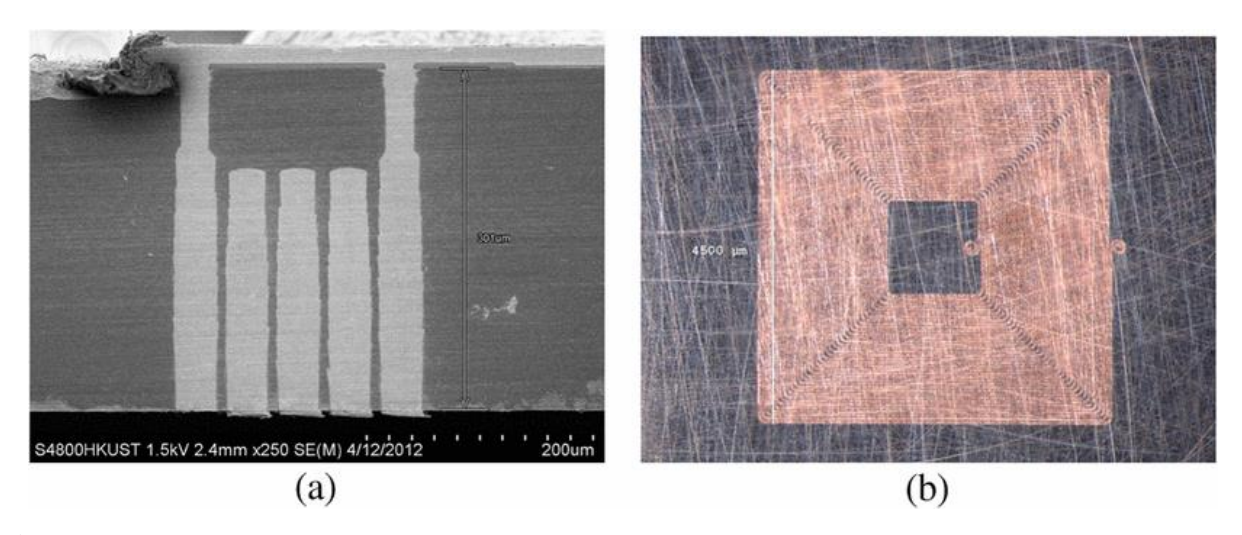


Figure 3.2: (a) Cross-sectional view of embedded Cu tracks and vias obtained from a testing structure. (b) Bottom view of the fabricated 4.5×4.5 mm² silicon-embedded receiving coil for wireless power transfer.

3.2.2 Experimental results

In this work, a wireless power link with an embedded power receiving coil was designed and fabricated, and the detailed design parameters are summarized in Table 3.1. The performance of the wireless power link with the embedded receiving coil and a PCB transmitting coil was characterized by measuring the 2-port S-parameters using an R&S ZVB8 vector network analyzer (VNA). Fig. 3.3 shows the detailed probing setup for a 2-port measurement of the wireless power link. The axial distance and lateral displacement between the coils is adjustable by tuning the screws.

TABLE 3.1

DESIGN PARAMETERS OF THE SILICON EMBEDDED WIRELESS POWER LINK

Specifications	PCB based primary power Silicon embedded secon	
	transmitting inductor	power receiving inductor
Outer radius	$r_{out_p} = 10 \text{ mm}$	$r_{out_s} = 2.25 \text{ mm}$
Track width	$w_p = 250 \; \mu \text{m}$	$w_s = 30 \ \mu \text{m}$
Track separation	$s_p = 250 \ \mu \text{m}$	$s_s = 15 \mu m$
Track thickness	$t_p = 30 \ \mu \text{m}$	$t_s = 200 \ \mu \text{m}$
Turn number	$n_P = 17$	$n_S = 37$
Inductor shape	Square	Square

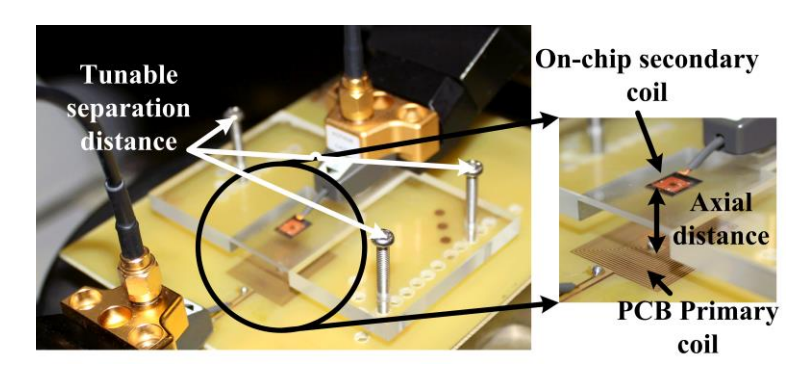


Figure 3.3: Detailed probing setup for two-port measurement of the wireless powering interface.

The electrical parameters (inductances and quality factor of both the power transmitting and receiving inductors and their mutual coupling) of the wireless power link were obtained from the 2-port measurement. Fig 3.4 shows the measured inductance and quality factor of the embedded power receiving coil at different frequencies. A large inductance of 4.0 µH and a high peak quality factor of 22 were achieved at 3 MHz. The self-resonant frequency was around 50 MHz. Fig 3.5 shows the measured self and mutual inductances for the wireless power link. The measured low-frequency inductance of the PCB power transmitting inductor was 3.3 µH. Low-frequency mutual inductances of 220 nH and 60 nH were obtained for axial distances of 5 mm and 12 mm, respectively. This corresponds to a coupling factor ranging from 0.06 to 0.016, respectively.

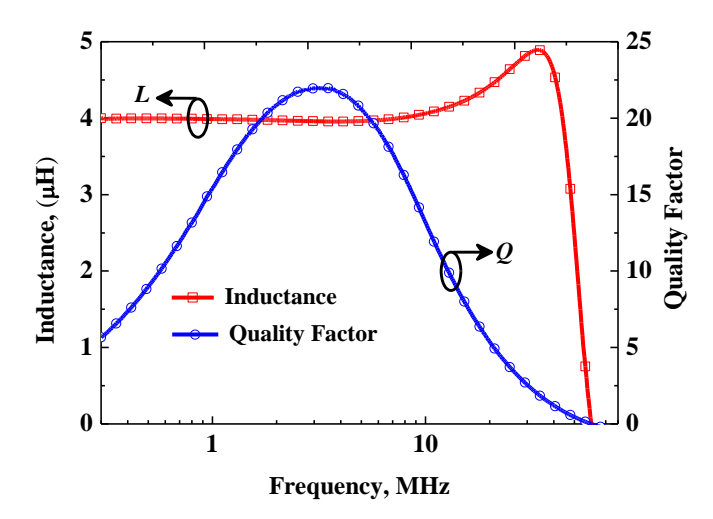


Figure 3.4: Measured inductance and quality factor of the embedded power receiving inductor.

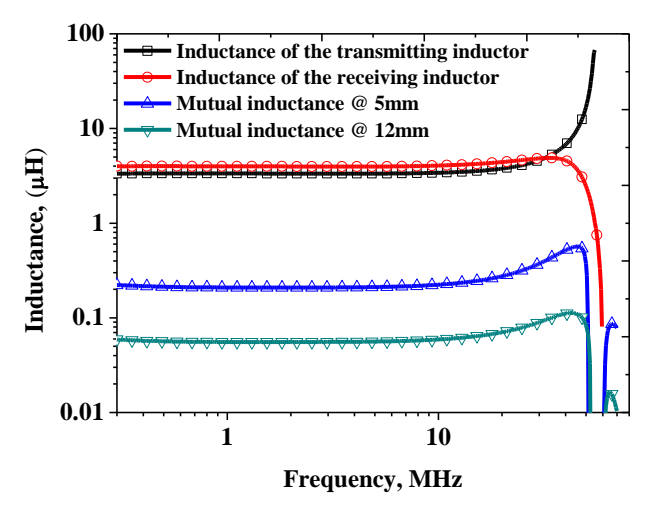


Figure 3.5: Measured inductances of the embedded power receiving coil and the PCB transmitting coil along with their mutual inductances at different separation distances (at 5 mm and 12 mm).

Fig. 3.6 shows the calculated maximum achievable efficiency of the wireless power link using (2.22). The maximum achievable efficiency varied with respect to the frequency. Fig 3.6 shows that the power link demonstrated its best performance at a frequency of about 6.78 MHz, which relies on the ISM band. At 6.78 MHz, the maximum efficiency can be obtained: 32% and 4.3% at axial separations of 5 mm and 12 mm, respectively. The performance of the wireless power link was investigated at different axial separations and lateral displacements. Fig 3.7(a) shows

the variation in the maximum efficiency at different separation distances. Fig 3.7(b) shows that the efficiency deteriorated drastically with the lateral displacement. And it can be outlined that 8 mm of lateral displacement is tolerable.

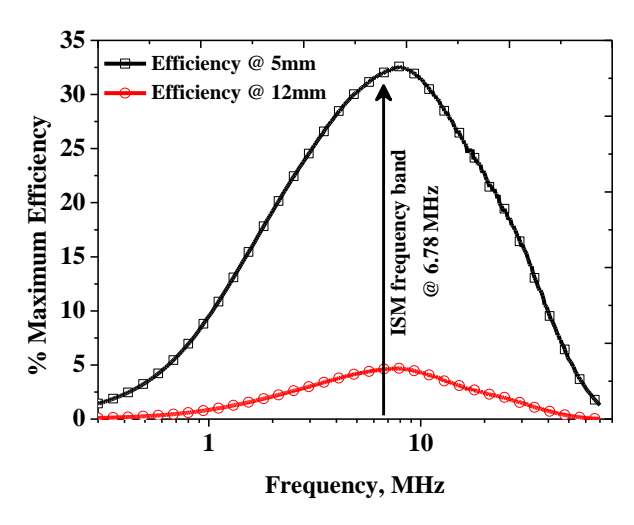


Figure 3.6: Measured maximum achievable efficiency at different frequencies.

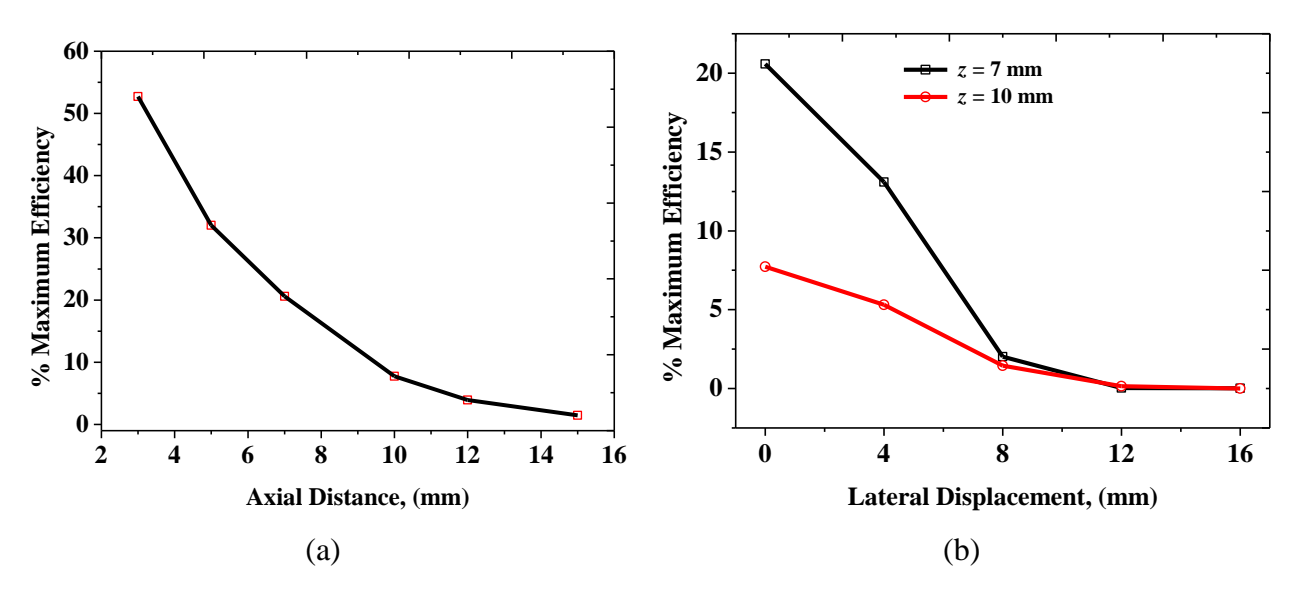


Figure 3.7: Measured maximum achievable efficiency at (a) different axial distances, and (b) lateral displacements while the operating frequency was at 6.78 MHz.

In practice, a load is always connected at the end of the wireless power link. According to (2.21), the variation of the load resistance also affects the efficiency of the wireless power link. The power link efficiency maximizes at an optimal load resistance. That's why another set of measurements was performed to find the optimal load resistance. To drive the power link in

resonance at 6.78 MHz, 167 pF and 138 pF capacitors were connected with the primary and the secondary inductor, respectively. The link efficiency was measured at different load resistances, as shown in Fig 3.8. These measurements were done at an axial separation of 10 mm. It was observed that a maximum efficiency of 7.7% was obtained at a load resistance of 2 K Ω .

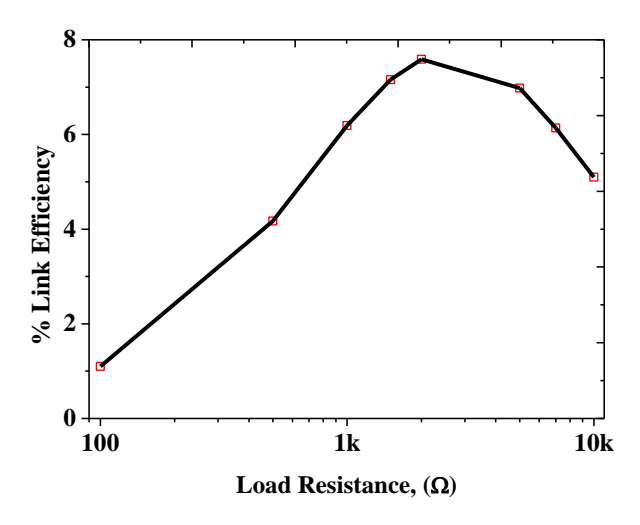


Figure 3.8: Variation in the efficiency of the wireless power link with different load impedances while the operating frequency was at 6.78 MHz and the axial distance was at 10 mm.

A silicon-embedded receiving coil has been designed and demonstrated for high-efficiency wireless power transfer to implantable biomedical ICs. The embedded power receiving coil achieved a large inductance of 4 μH and a high quality factor of 20. With this integration technique, excellent power efficiency was achieved. However, this silicon embedded inductor integration is only suitable for highly resistive substrates (> 1000 Ω • cm). For low resistivity wafers (10–30 Ω • cm), the quality factor deteriorates due to the induced eddy current in the highly conductive substrate. The fabricated embedded inductors in a low resistivity substrate possessed a very poor quality factor of 2~5 [18]. Therefore, the suitable applications of this embedded integration technique only exist in processes with highly resistive wafers, such as GaN-on-Si epitaxial wafers and SOI wafers.

3.3 Above CMOS inductor (ACI) integration technique

This section outlines a CMOS compatible on-chip inductor integration approach which can accommodate large value inductors without affecting the area of active circuitry. With this

methodology, an inductor was fabricated above the passivation layer of the CMOS chip. Thick SU8 dielectric film ($\epsilon r \approx 2.8$) was placed between the CMOS passivation layer and the inductor. SU8 film was also used to fabricate the inductor. SU8 is easily patternable by photolithography, and after being cured by hard baking, it served the purpose of a dielectric. In the process of the inductor fabrication, SU8 was patterned to create deep trenches, and then these deep trenches were filled with copper by a damascene process. Since a low-k dielectric material was placed beneath the inductor, the substrate loss was significantly reduced, and the inductor showed superior performance (higher quality factor and inductance density) irrespective of the resistivity of the substrate.

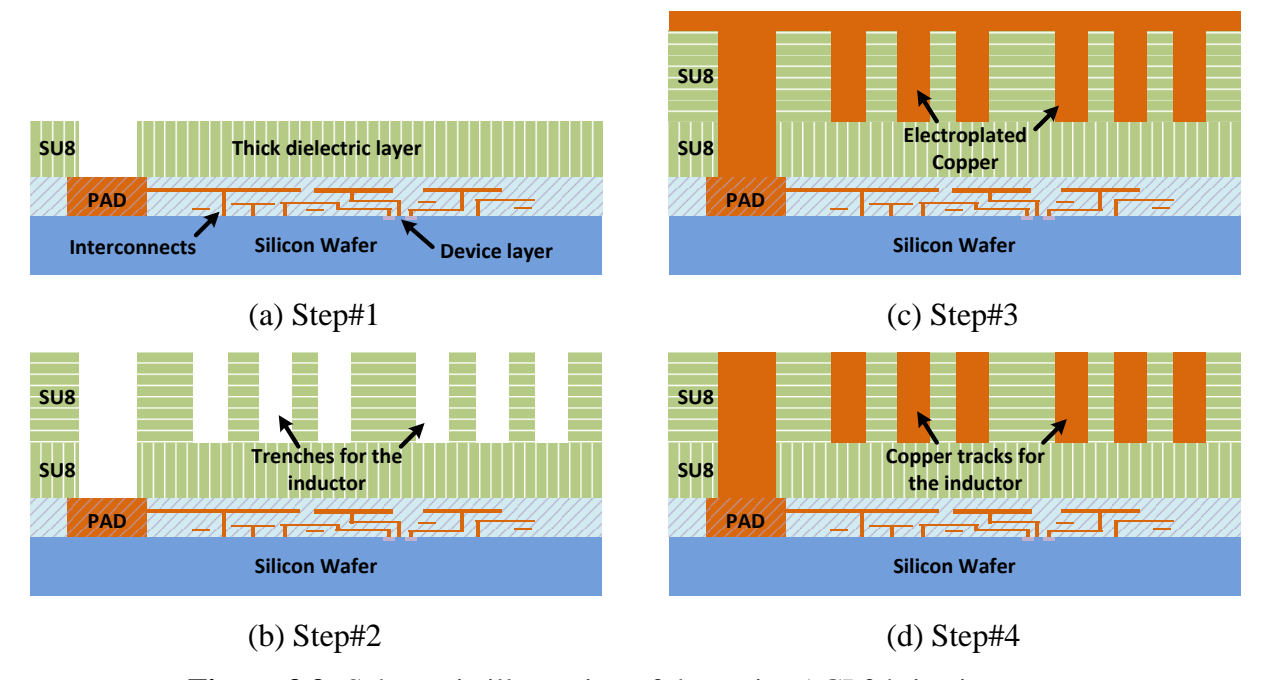


Figure 3.9: Schematic illustration of the major ACI fabrication steps.

3.3.1 The power receiving inductor fabrication using ACI technology

Fig. 3.9 illustrates the detailed fabrication steps for the power receiving inductor using the ACI integration technology. A thick (\sim 10 μ m) dielectric layer was placed on top of the interconnect layer of the CMOS chip. During this process step, the passivation layer on top of the PAD was removed. Then, trenches about 50 μ m deep , which were used as the inductor's tracks, were created by photolithography. 50 nm Ti/W and 2 μ m Cu were then sputtered on top of the trenches as the seed layer, followed by acid copper electroplating using a small dc current density of 0.5 mA/cm². After this process step, all trenches were filled with electroplated Cu, as

shown in Fig 3.10(a). Then, the over-plated Cu was removed by polishing. Fig 3.10(b) and (c) show the cross-sectional and top views of the fabricated inductor. The geometric parameters of the power receiving inductor are summarized in Table 3.2,

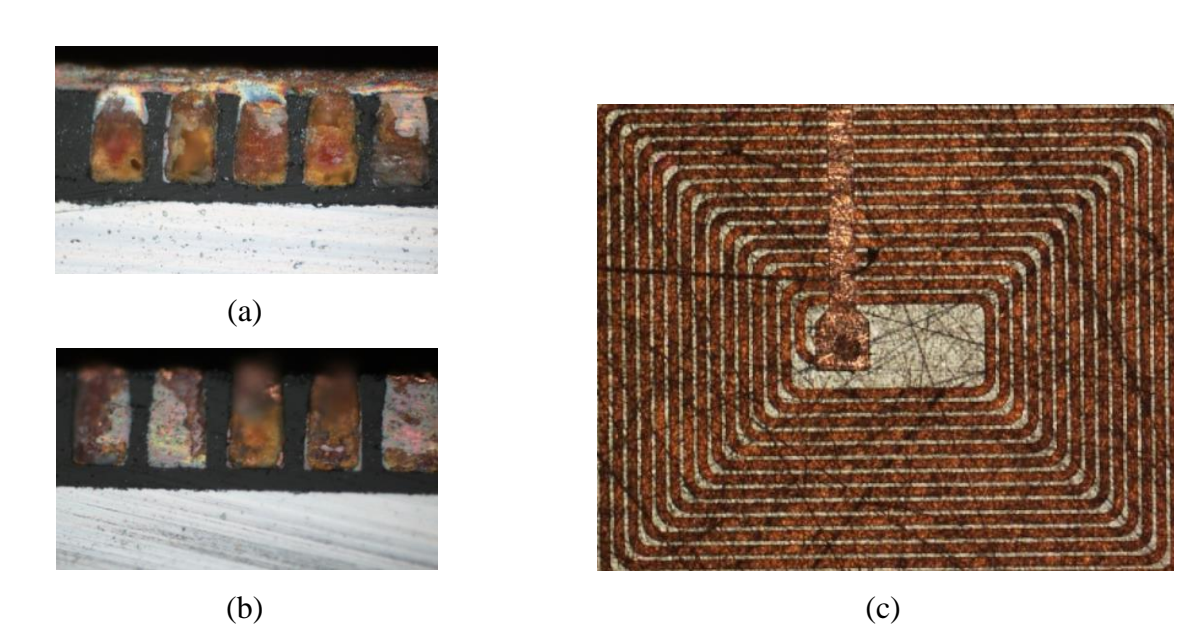


Figure 3.10: (a) SEM images of trenches for the inductor, which are filled by electroplated Cu. (b) Cross-sectional view of Cu tracks of the inductor. Over-plated Cu was removed by polishing. (c) Plane view of the fabricated inductor.

3.3.2 A wireless power link prototype using ACI technology and characterization

A prototype of the wireless power link was established using the ACI integrated power receiving inductor. The design parameters of the wireless link are shown in Table 3.2. A detailed probing setup for the 2-port s-parameter measurement of the power link is shown in Fig. 3.3. The measured electrical parameters of the ACI integrated power receiving coil are shown in Fig 3.11. A peak quality factor of 22 was obtained at a frequency of about 10 MHz. The substrate resistivity was 10 Ω • cm. This low resistivity of the substrate did not affect the quality factor of the inductor as there was a 10 μ m thick isolation layer placed in between the inductor and the substrate. The obtained DC inductance was 4.3 μ H, and the inductance density was 210 nH/mm². The PCB based primary coil in this prototype is similar to that described in Section 3.2.2. From the 2-port s-parameter measurement, the maximum achievable efficiency was evaluated, as shown in Fig 3.12. Fig 3.12 shows that the efficiency varies over different frequencies; it

maximizes a frequency of around 10 MHz. At the ISM frequency band of 13.56 MHz, it shows a peak efficiency of 37% and 8% at the axial distances of 5mm and 10mm, respectively.

TABLE 3.2

DESIGN PARAMETERS OF THE ACI INTEGRATED WIRELESS POWER LINK

Specifications	PCB based primary power	ACI intenerated secondary
	transmitting inductor	power receiving inductor
Outer radius	$r_{out_p} = 10 \text{ mm}$	$r_{out_s} = 2.25 \text{ mm}$
Track width	$w_p = 250 \; \mu \text{m}$	$w_s = 25 \mu \text{m}$
Track separation	$s_p = 250 \ \mu \text{m}$	$s_s = 20 \ \mu \text{m}$
Track thickness	$t_p = 30 \ \mu \text{m}$	$t_s = 40 \ \mu \text{m}$
Turn number	$n_P = 17$	$n_S = 35$
Inductor shape	Square	Square

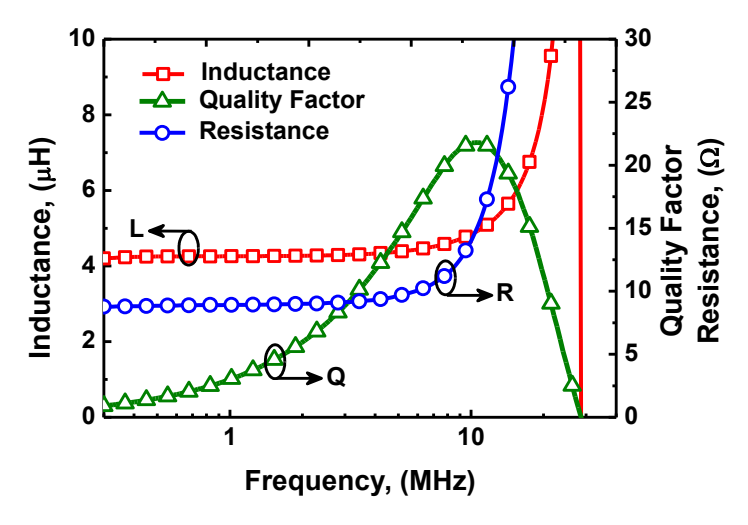


Figure 3.11: Measured inductance, quality factor and series resistance of the ACI integrated power receiving coil.

Another set of measurements was performed at different axial separations while the frequency was set at 13.56 MHz. Fig 3.13 shows the variation in the maximum efficiency at different axial distances. Also, the link efficiency and the voltage gain of the wireless power link were investigated with respect to the load resistance. In these measurements, 40 pF and 27 pF capacitors were connected with the primary and the secondary coil, respectively, in order to

achieve resonance at a frequency of 13.56MHz. These capacitors can easily be integrated with a CMOS chip using the standard fabrication process. Fig 3.14 shows that the link efficiency maximized at a load resistance of 7 K Ω . At that load, the voltage gain was about 0.2. According to these results, at 13.56 MHz, 24.7 V_{RMS} is required at the primary transmitting coil to supply 1 mW power at the load of the power receiving side at a separation distance of 10mm.

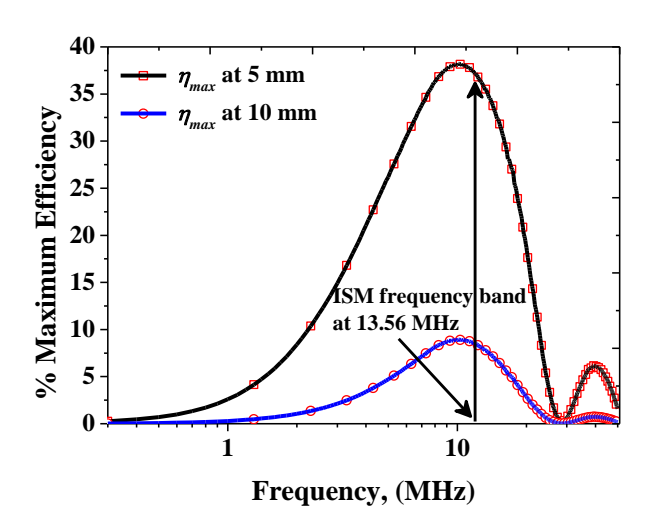


Figure 3.12: Maximum achievable efficiency of the ACI integrated wireless power link at different frequencies.

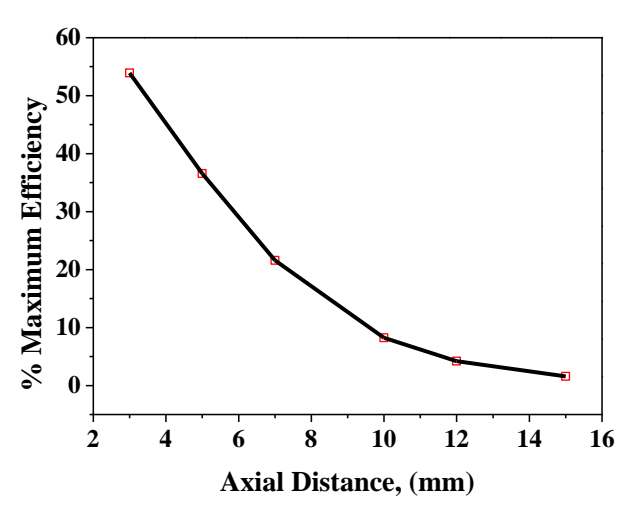


Figure 3.13: Maximum efficiency of the ACI integrated wireless power link at different axial distances.

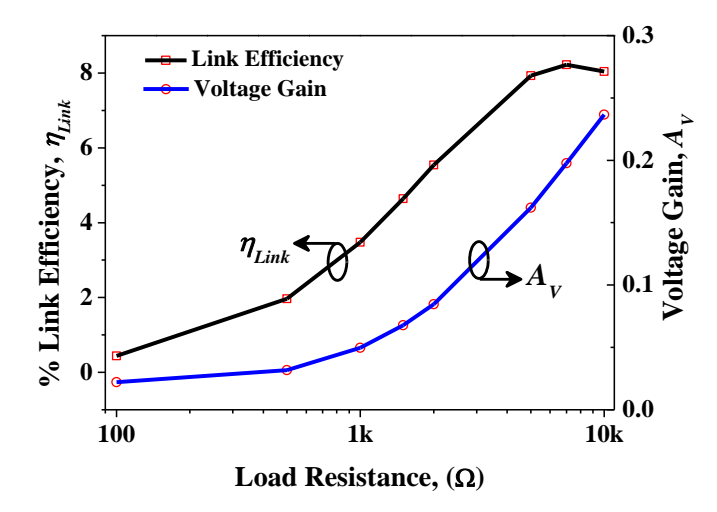


Figure 3.14: Measured link efficiency and voltage gain of the ACI integrated wireless power link at different load resistances. These measurements were done at 10 mm axial distance.

In this section, an above-CMOS inductor (ACI) integration process has been proposed for high efficiency wireless power transfer applications. A power receiving coil was fabricated using ACI technology. Inductors with a high quality factor (> 20) and large inductance density (> 200 nH/mm²) can be achieved using this technology. Fewer process steps are required as the SU8 film can be patterned by photolithography. This simple process is highly compatible with standard IC fabrication. Because of the superior performance of the ACI integrated power receiving coil, the wireless power link can transmit energy with a very good link efficiency of 37% at a distance of 5 mm.

3.4 Characterization of the wireless power link in a bio-environment

In practice, bio-microsystems are placed inside the body. Because the behavior of the wireless power link might be changed within a bio-environment, the changes need to be characterized. In this section, the electrical parameters of wireless power links were measured inside a tissue environment. Fig. 3.15 shows the experimental setup for characterizing the system in a bio-environment. Muscle tissue was placed between the primary and the secondary coil, and a 0.5 mm thin plastic layer was used for isolation in order to avoid any damage to the measurement equipment and the DUT.

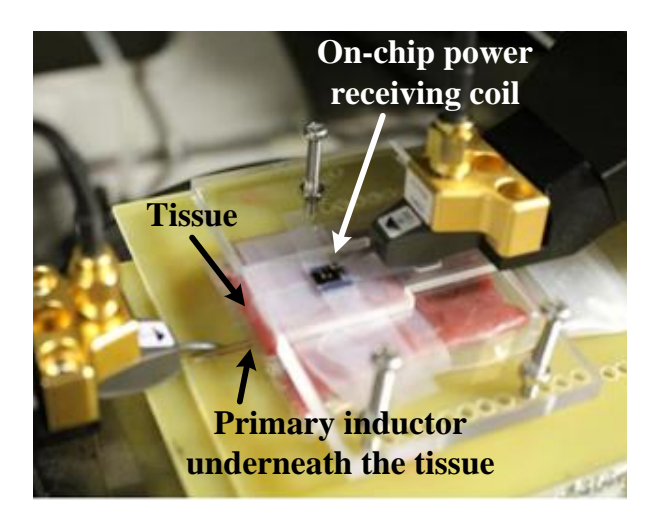


Figure 3.15: Experimental setup for measuring the wireless power link properties in a bio-environment.

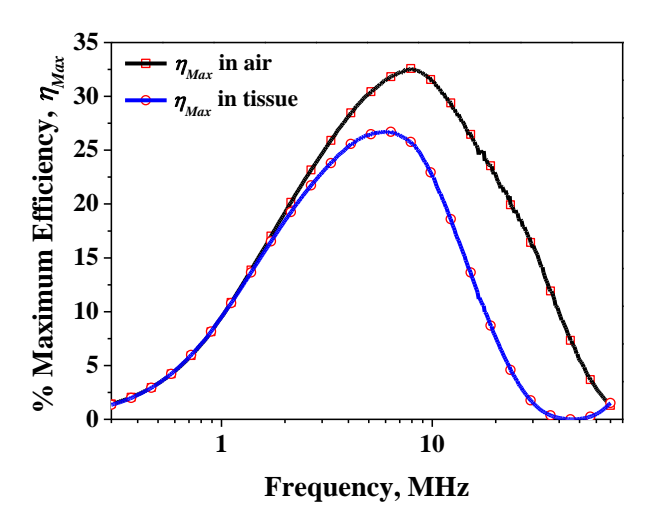


Figure 3.16: Comparison between the measured efficiency of the power link in air and a bio-environment while the spacing between the primary and the secondary coil was fixed at 5 mm.

The 2-port s-parameter measurement was performed, and the maximum efficiency was calculated, as shown in Fig. 3.16. At a low frequency, the performance of the power link in the bio-environment was similar to that in the air. But, at a high frequency the performance significantly deteriorated. For example, the peak efficiency at a frequency of 6.78 MHz decreased from 32% to 27% (for a 5 mm separation distance) when the link was shifted inside the tissue. At a high frequency, the tissue induced eddy current loss to the inductor as the muscle tissue has a resistivity of about 200 Ω • cm [19] and the dielectric permittivity is about 10[20]. As a result, the quality factor of both the primary and the secondary coil was decreased, as

shown in Fig 3.17. However, the tissue environment did not affect the self and mutual inductances. The deterioration of the quality factor was the primary reason behind the efficiency degradation of the wireless power link inside the tissue environment.

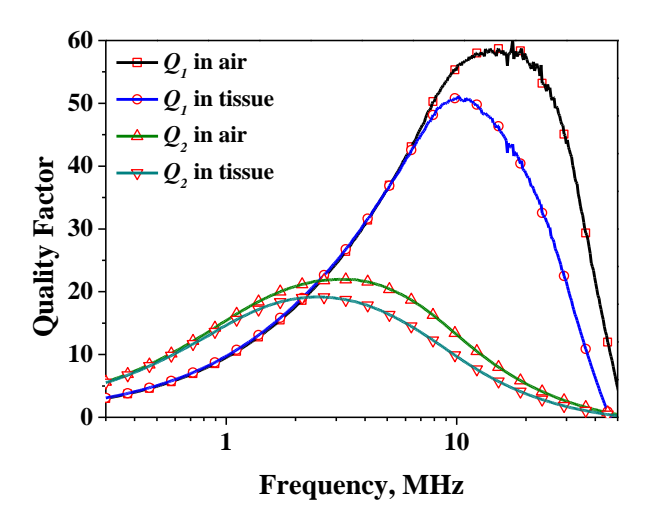


Figure 3.17: Comparison between the quality factors obtained in the air and bio-environment. Q_1 refers to the quality factor of the primary transmitting coil and Q_2 is for the secondary power receiving coil.

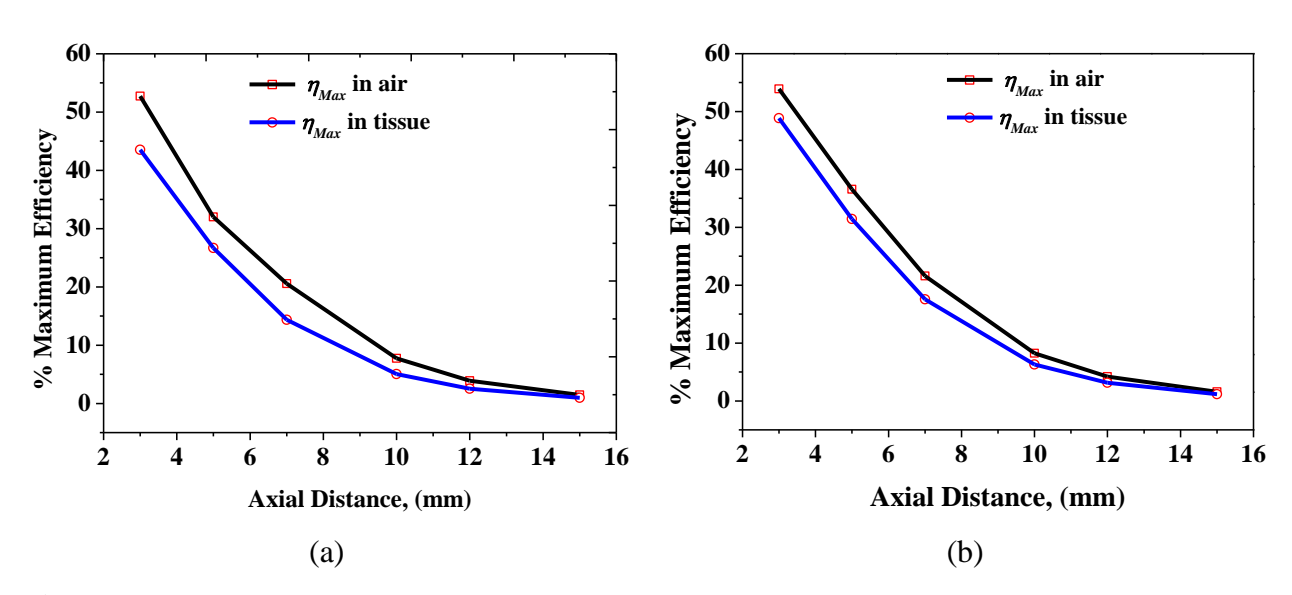


Figure 3.18: Variations in peak efficiency of the wireless power link in different operating environments (air or tissue) with various coupling distances. (a) Silicon embedded power receiving coil at a frequency of 6.78 MHz. (b) ACI integrated power receiving coil at a frequency of 13.56 MHz.

Both, the silicon embedded and above-CMOS inductor integration based wireless power links were measured in the tissue environment. Fig. 3.18 shows the comparison between the measured efficiencies in the air and in the bio-environment at different separation distances. Because of the bio-environment, about 10~15% efficiency degradation was observed in both of these two wireless power links.

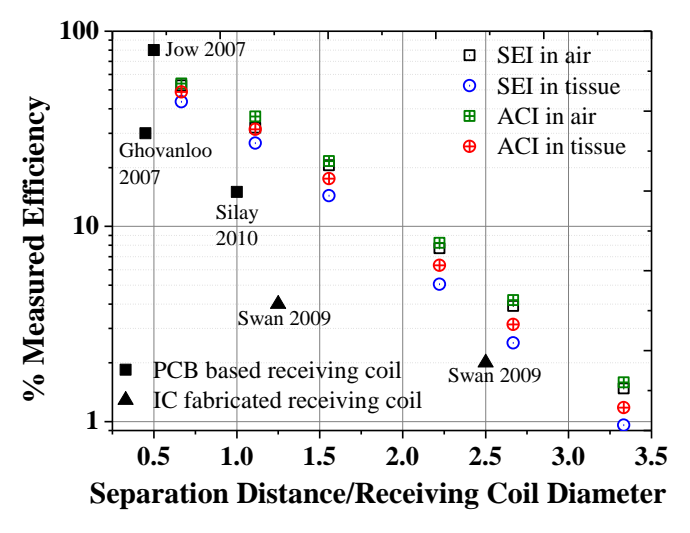


Figure 3.19: Comparison of the wireless power link efficiency with prior arts. **SEI:** Silicon Embedded Inductor and **ACI:** Above-CMOS Inductor.

Fig. 3.19 compares the efficiency of the wireless power link using the proposed on-chip power receiving coil technologies with previously reported power link prototypes [6-10]. The separation distance normalized to coil size is also indicated for a fair comparison. In this work, the receiving coil diameter is only 4.5 mm, which is the typical dimension of a bio-microsystem [4], [5]. The power link with the embedded receiving inductor showed better performance than any of the other reported prototypes. However, the embedded technology showed such better performance only for a high resistivity substrate. In contrast, measurement results suggest that the ACI integrated technology showed superior performance to any other technology, even when the substrate resistivity was as low as $10 \ \Omega \cdot cm$.

References

- [1] R.R. Harrison, "Designing efficient inductive power links for implantable devices," *IEEE International Symposium on Circuits and Systems*, New Orleans, USA, May 2007, pp. 2080-2083.
- [2] M.V. Paernel, "High-efficiency transmission for medical implants," *IEEE Solid-State Circuits Magazine*, vol. 3, no. 1, pp. 47-59, 2011.
- [3] R.R. Harrison *et al.*, "A low-power integrated circuit for a wireless 100-electrode neural recording system," *IEEE Journal of Solid-State Circuits*, vol. 42, no. 1, pp. 123-133, 2007.
- [4] H. Hori et al., "The thickness of human scalp: normal and bald," *Journal of Investigative Dermatology*, vol. 58, no. 6, pp. 396-399, 1972.
- [5] "Study: women's skulls thicker, men's wider; might affect protection design," *Occupational Health & Safety*, January 2008.
- [6] U.-M. Jow and M. Ghovanloo, "Design and optimization of printed spiral coils for efficient transcutaneous inductive power transmission," *IEEE Transactions on Biomedical Circuits and Systems*, vol. 1, no. 3, pp. 193-202, 2007.
- [7] M. Ghovanloo and S. Atluri, "A wide-band power-efficient inductive wireless link for implantable microelectronic devices using multiple carriers," *IEEE Transactions on Circuits and Systems-I: Regular Papers*, vol. 54, no. 10, pp. 2211-2221, 2007.
- [8] G. Simard *et al.*, "High-speed OQPSK and efficient power transfer through inductive link for biomedical implants," *IEEE Transactions on Biomedical Circuits and Systems*, vol. 4, no. 3, pp. 192-200, 2010.
- [9] K.M. Silay *et al.*, "Inductive power link for a wireless cortical implant with biocompatible packaging," *IEEE Sensors Conference*, Kona, USA, November 2010, pp. 94-98.
- [10] M. Sawan et al., "Multicoils-based inductive links dedicated to power up implantable medical devices: modeling, design and experimental results," *Biomedical Microdevices*, vol. 11, no. 5, pp. 1059-1070, 2009.
- [11] S. Kim *et al.*, "Switchable polymer-based thin film coils as a power module for wireless neural interfaces," *Sensors and Actuators A*, vol. 136, no.1, pp. 467-474, 2007.
- [12] C. O'Mathuna, *et al.*, "Review of integrated magnetics for power supply on chip (PwrSoC)," *IEEE Transactions on Power Electronics*, vol. 27, no. 11, pp. 4799-4815, 2012.

- [13] P.T. Theilmann and P.M. Asbeck, "An analytical model for inductively coupled implantable biomedical devices with ferrite rods," *IEEE Transactions on Biomedical Circuits and Systems*, vol. 3, no. 1, pp. 43-52, 2009.
- [14] R. Wu and J. K. O. Sin, "A novel silicon-embedded coreless inductor for high-frequency power management applications," *IEEE Electron Device Letters*, vol. 32, no. 1, pp. 60-62, 2010.
- [15] R. Wu *et al.*, "Wireless power link design using silicon-embedded inductors for brain-machine interface," *International Symposium on VLSI Design, Automation and Test*, Hsinchu, Taiwan, April 2012.
- [16] R. Wu and J.K.O. Sin, "High efficiency silicon-embedded coreless coupled inductors for power supply on chip applications," *IEEE Transactions on Power Electronics*, vol. 27, no. 11, pp. 4781-4787, 2012.
- [17] R. Puschmann *et al.*, "Via last technology for direct stacking of processor and flash," *IEEE Electronic Components and Technology Conference*, San Diego, USA, May 2012, pp. 1327-1332.
- [18] R. Wu, J. K. Sin, and C. P. Yue, "High-Q Backside Silicon-Embedded Inductor for Power Applications in uH and MHz Range," *IEEE Transactions on Electron Device*, vol. 60, no. 1, pp. 339-345, Jan. 2013.
- [19] Stanley Rush, J.A. Abildskov, and Richard McFee, "Resistivity of Body Tissues at Low Frequencies," *Circulation Research*, Volume XII, January 1963.
- [20] C Gabriel, S Gabriel and E Corthout, "The dielectric properties of biological tissues: I. Literature survey," *Phys. Med. Biol.* Vol. 41, April 1996.

Chapter 4

Demonstration of a complete wireless power transfer system

4.1 Detailed measurement setup of the demonstration

A complete wireless power transmission system requires a power management system which converts the wirelessly-coupled RF signal into a stable DC supply voltage. This DC source works as supply to support the functionality of a bio-microsystem. Fig. 4.1 describes a complete wireless power delivery system. RF power is transmitted from the primary transmitting coil (L_I) to the secondary power receiving coil (L_2), and then the rectifier converts that coupled RF signal to a usable DC source [1-4]. This unregulated DC supply may be further adjusted using a power regulator [5-6].

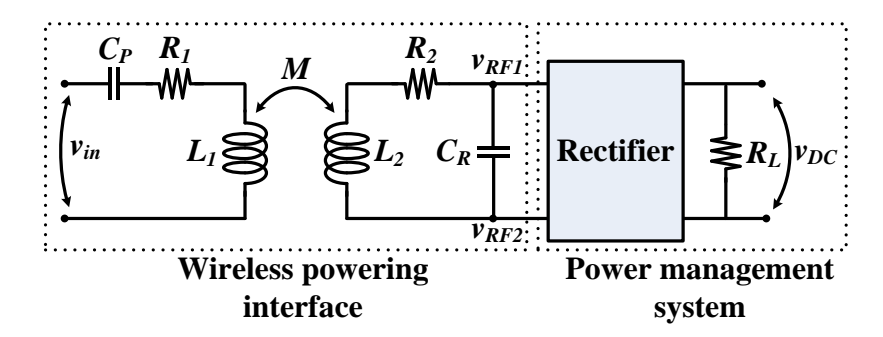


Figure 4.1: Complete schematic diagram of a wireless power delivery system

A complete wireless power transfer system was demonstrated using a CMOS fabricated rectifier chip¹, shown in Fig. 4.2(a). Above CMOS inductor technology was followed to fabricate the power receiving inductor. The available area for the receiving inductor, which is 1.3×1.06mm², is identified in Fig. 4.2(a). A test inductor was fabricated using the same area, as shown in Fig. 4.2(b). The demonstration was done using this test structure as the fabrication process is still going on. The test inductor was connected with the CMOS chip using bond-wire, as shown in Fig. 4.4.

The CMOS chip contains a rectifier and a tuning capacitor ($C_R = 90$ pF). The system was designed to operate at an ISM frequency band of 40.68 MHz. To maximize the power efficiency

¹Special thanks to Professor Chi-Ying TSUI and Xing LI for allowing me to use their fabricated chip for my system demonstration.

of the system at a certain frequency, the system needs to be operated at resonance [7]. That's why about 170 nH of inductance was required for the secondary power receiving coil to achieve resonance at a frequency of 40.68 MHz. The inductance of the fabricated inductor was 174 nH and the quality factor about 18. The primary power transmitting side also needed to be resonated at the same frequency. The inductance of the primary coil was 250 nH, and the tuning capacitor (C_P) was set at 62 pF to resonate at 40.68 MHz.

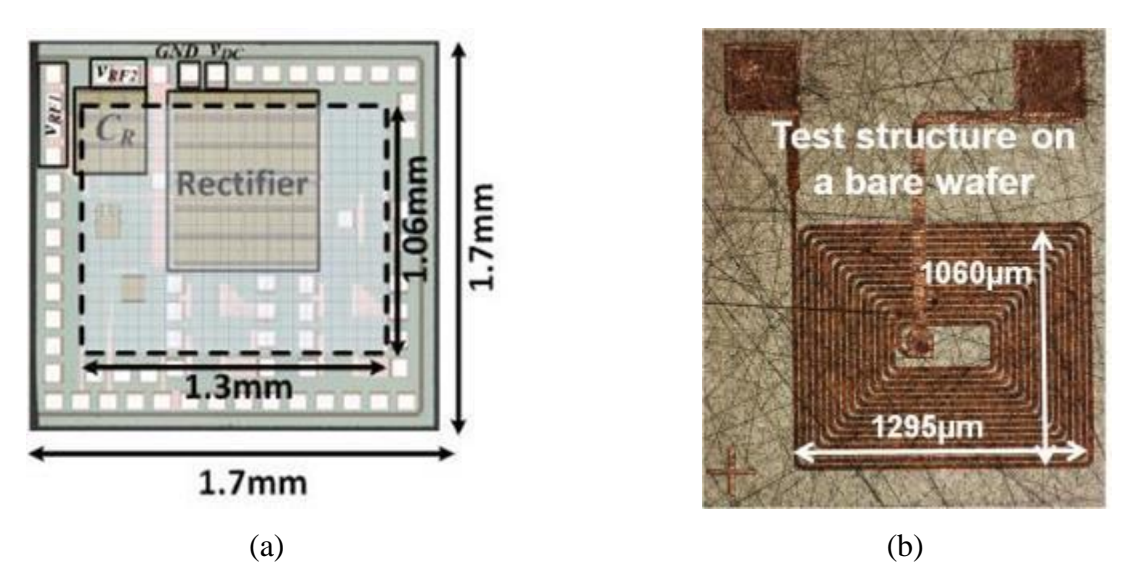


Figure 4.2: (a) The chip micrograph of a retinal implant containing a rectifier and a secondary tuning capacitor ($C_R = 90$ pF). The area of the rectifier and the tuning capacitor are identified. Also, available space for an above-CMOS inductor is also outlined; it is about 1.3×1.06 mm².

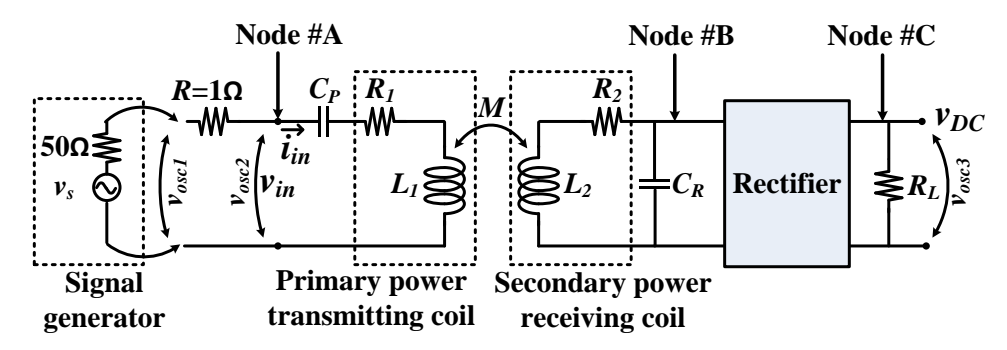


Figure 4.3: A conceptual schematic diagram of the measurement setup.

Fig. 4.3 shows a conceptual schematic diagram of the measurement setup. This measurement setup was done for the time domain measurement of the system. A signal generator supplied a continuous sinusoidal signal to the primary power transmitting coil. In order to measure the input

power to the primary side, simultaneous voltage and current signals needed to be observed. Two high impedance oscilloscope probes were used to observe the voltage across the signal generator and at node A, as shown in Fig. 4.3. The input voltage of the primary side was measured by v_{osc2} , i.e. $(v_{in} = v_{osc2})$, and the input current i_{in} was measured as $i_{in} = (v_{osc1} - v_{osc2})/R$. From these measurements, the input power to the primary side can be calculated as

$$P_{in} = \frac{1}{t_2 - t_1} \int_{t_1}^{t_2} v_{in}(t) \times i_{in}(t) dt.$$
 (4.1)

At the power receiving side, another high impedance probe was used to measure the received DC voltage at the load end ($v_{DC} = v_{osc3}$). And the received power was calculated as

$$P_{out} = \frac{v_{DC}^2}{R_I}.$$
 (4.2)

And the total system efficiency from node A to node C was calculated as $\eta_{A-C} = 100 \times \frac{P_{out}}{P_{in}}$.

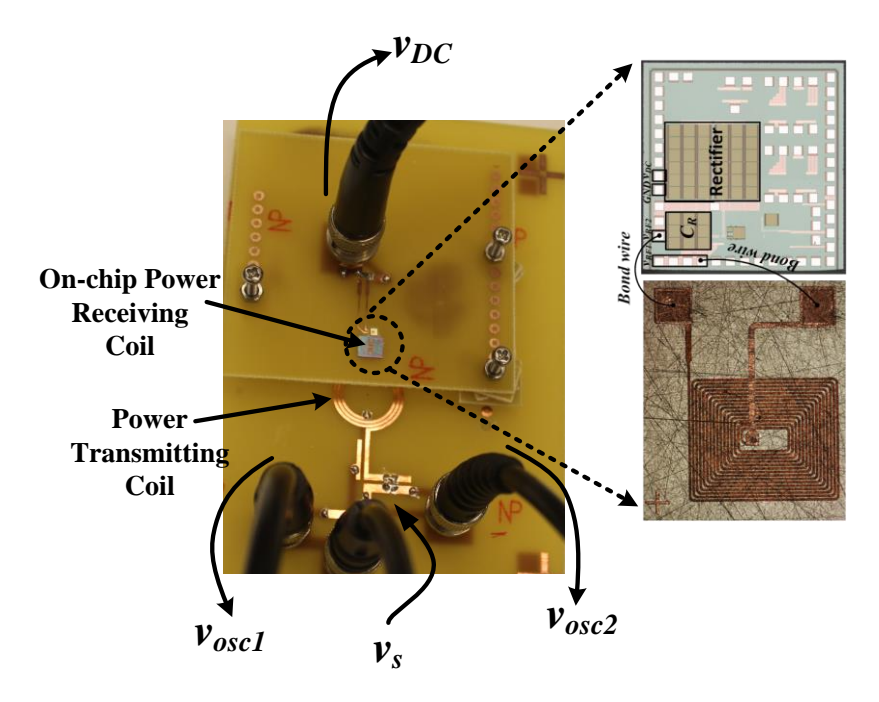


Figure 4.4: The demonstration setup of the complete wireless power transfer system.

4.2 Performance of the power transfer system

The complete demonstration setup of the wireless power transfer system is shown in Fig. 4.4. Three types of wireless power links were setup and measured for the demonstration, as described

in Table 4.1. Initially, a 2-port s-parameter measurement was done to investigate the power link performance from node A to node B. The electrical parameters of the individual coil and the performance of the power link are also summarized in Table 4.1.

TABLE 4.1

PARAMETERS OF WIRELESS POWER DELIVERY SYSTEMS CONSTRUCTED BY DIFFERENT SIZES OF
INDUCTORS

Specifications	Primary Coil	Secondary Coil	Secondary Coil	Secondary Coil
		(On-PCB)	(On-PCB)	(On-Chip)
Turn Number	3	2	4	15
Track Width	700 μm	500 μm	3	3
Track Spacing	300 μm	300 μm	700 μm	700 μm
Coil Area	$20\times20~\text{mm}^2$	20×20 mm ²	10×10 mm ²	$1.06 \times 1.3 \text{ mm}^2$
/ Shape	/ Circular	/ Circular	/ Circular	/ Rectangular
Inductance	250 nH	169 nH	171 nH	174 nH
Quality Factor	132	116	82	18
η_{A-B} (From s-	~	88%	16%	1.35%
parameter		(at 10 mm	(at 10 mm	(at 10 mm
measurement)		distance)	distance)	distance)

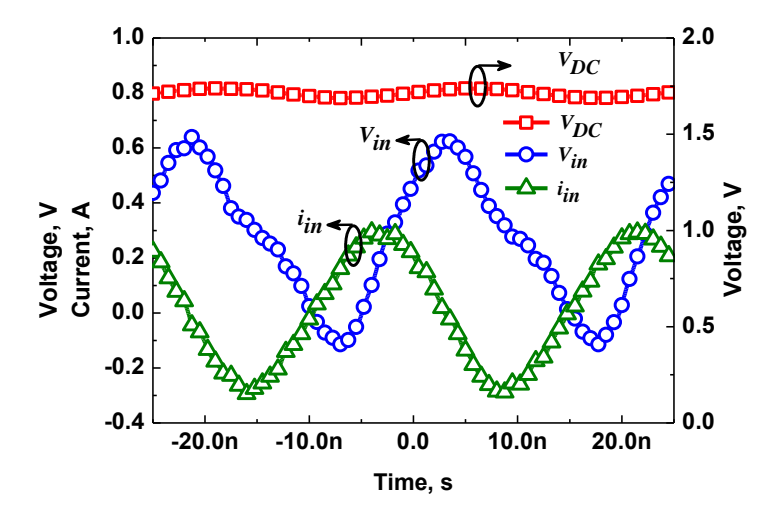


Figure 4.5: Time domain measurement of v_{in} , i_{in} and v_{DC} .

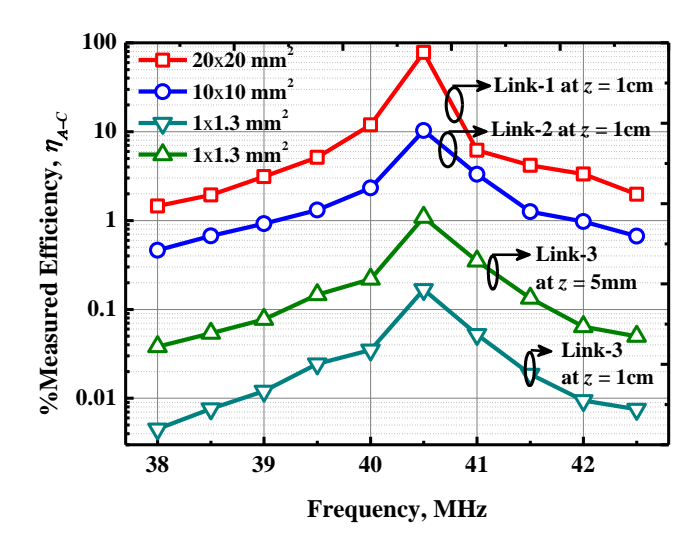


Figure 4.6: Measured total system efficiency (η_{A-C}) at different frequencies.

Fig. 4.5 shows the measured input voltage and current at the primary power transmitting coil. The received signal at node B was not measured as there was a possibility of affecting the performance of the rectifier. The rectifier converted the received AC signal to usable DC voltage, as shown in Fig. 4.5. The nominal efficiency of the rectifier was 80%. In all of the three cases (for Links 1, 2 and 3), a fixed resistance of 1 K Ω was connected to the rectifier as a load resistance (R_L =1 K Ω). During the time domain measurement, the frequency of the signal generator was tuned to find out the resonant frequency of the system. Fig. 4.6 shows that the total efficiency of the power transfer system was maximized at the resonance frequency. All these measurements were done at a separation distance z of 1 cm.

For the smaller power receiving coil, lower efficiency was expected. For fair comparison, a term, received power density ($P_{Density}$), was allocated, which is defined as

$$P_{Density} = P_{in} \times \frac{\eta_{A-C}}{S_{Area}} \,. \tag{4.3}$$

Here, the S_{Area} is defined as the total area occupied by the power receiving system.

TABLE 4.2

COMPARISON OF RECEIVED POWER DENSITY AMONG DIFFERENT TYPES OF WIRELESS POWER

TRANSMISSION SYSTEMS

Transmitted power by the Primary	Secondary	Secondary	Secondary
$coil, P_{in} = 100 \text{ mW}$	(On PCB)	(On PCB)	(On-Chip)
	Link-1	Link-2	Link-3
Area	20×20 mm ²	10×10 mm ²	$1.06 \times 1.3 \text{ mm}^2$
Received power density ($P_{Density}$)	$194 \mu W/mm^2$	$103 \mu \text{W/mm}^2$	$128\mu W/mm^2$
at 1cm separation			

Table 4.2 summarizes the received power density of different power links. Even though the efficiency of the on-chip fabricated receiving coil was less than the PCB based coils, the received power density was comparable. When the transmitted power was 100mW, the received power density at the on-chip secondary receiving coil was about 128μW/mm², which is sufficient for powering any typical bio-microsystem [6], [8-9].

References

- [1] Lu Yan, Xing Li, W. H. Ki, CY Tsui and C. P. Yue, "A 13.56MHz Fully Integrated 1x/2x Active Rectifier with Compensated Bias Current for Inductively Powered Devices," *IEEE International Solid-State Circuits Conference Digest of Technical Papers (ISSCC)*, pp. 66-67, Feb 2013.
- [2] Y. Lu, W.-H. Ki, and J. Yi, "A 13.56MHz CMOS Rectifier with Switched-Offset for Reversion Current Control," *IEEE Symp. VLSI Circuits*, pp. 246-247, June 2011.
- [3] H.-K. Cha, W.-T. Park, and M. Je, "A CMOS Rectifier with a Cross-Coupled Latched Comparator for Wireless Power Transfer in Biomedical Applications," *IEEE Trans. Circuits and Systems-II*, vol. 59, no. 7, pp. 409-413, Jul. 2012.
- [4] H. Lee and M. Ghovanloo, "An Adaptive Reconfigurable Active Voltage Doubler/Rectifier for Extended-Range Inductive Power Transmission," *ISSCC Dig. Tech. Papers*, pp. 286-287, Feb. 2012.

- [5] K. Chen, Z. Yang, L. Hoang, et al., "An Integrated 256-Channel Epiretinal Prosthesis," *IEEE J. Solid-State Circuits*, vol. 45, no. 9, pp. 1946-1956, Sept. 2010.
- [6] W. Biederman, et al., "A fully-integrated 10.5μW miniaturized (0.125mm²) wireless neural sensor," *IEEE J. Solid-State Circuits*, vol. 48, no. 4, pp. 960 970, April 2013.
- [7] R. Jegadeesan, and G. Yong-Xin, "Topology Selection and Efficiency Improvement of Inductive Power Links," IEEE Transactions on Antennas and Propagation, vol. 60, no. 10, pp. 4846 - 4854, Oct. 2012.
- [8] L. S. Y. Wong, S. Hossain, A. Ta, J. Edvinsson, D. H. Rivas and H. Naas, "A very low-power CMOS mixed-signal IC for implantable pacemaker applications," *IEEE J. Solid-State Circuits*, vol. 39, no. 12, pp. 2446-2456, 2004.
- [9] J. S. Ho, S. Kim, and S. Y. Poon, "Midfield Wireless Powering for Implantable Systems," *Proceedings of the IEEE*, vol. 101, no. 6, pp. 1369 1378, June 2013.

Chapter 5

Conclusion

5.1 Summary of contributions

A compact model for a wireless power link, by which link efficiency and voltage gain can be predicted at different operating conditions, was developed. The proposed model does the prediction from the geometric parameters of planar inductors and the relative placement of them. An inductive power link was implemented, and the effectiveness of the model was investigated by comparing the measured and calculated results. This model can also estimate the optimal operating frequency and load for maximal power transfer. In practice, these are the most important design parameters.

This work outlined CMOS compatible on-chip inductor integration approaches to integrate bio-microsystems and the power delivery interface on a single chip. The first approach was silicon embedded technology. Using this technology, a 4.5×4.5 mm² power receiving inductor was fabricated in a highly resistive silicon wafer. The measured power link showed better power transfer efficiency compared to any other reported prototypes. However, this technology is only suitable for high resistivity substrates. Another integration approach, above-CMOS integration (ACI), was proposed to realize a fully integrated power delivery interface. Using this approach, the power delivery interface also showed excellent performance; most importantly, the performance does not degrade due to a low resistivity substrate.

Using this ACI integration technique, an operating wireless power delivery interface was demonstrated. The size of the receiving coil was only $1.06\times1.3~\text{mm}^2$. The demonstration showed a receiving power density of $128\mu\text{W/mm}^2$, while a typical bio-implanted device requires only $100~\mu\text{W}$ to support its full functionality.

5.2 Directions of future research

Although, this work provides a complete model of a wireless power link, an algorithm needs to be developed to design a highly efficient power link. The performance of the wireless power link changes when it is placed inside a bio-environment. The model could be improved in future to capture the variation in performance within such an environment.

Publications

- [5] S. Raju, R. Wu, M. Chan and C. P. Yue "Modeling of mutual coupling between planar inductors in wireless power applications," *IEEE Transaction on Power Electronics*, vol. 29, no. 1, pp. 481–490, Jan. 2014.
- [4] R. Wu, S. Raju, M. Chan, J. K.O. Sin and C. P. Yue, "Silicon-Embedded Receiving Coil for High-Efficiency Wireless Power Transfer to Implantable Biomedical ICs," *IEEE Electron Device Letters*, vol. 34, no. 1, pp. 9–11, Jan. 2013.
- [3] S. Raju, M. Chan and C. P. Yue, "Modeling of an Inductive Link for Wireless Power Applications," *IEEE International conference on Electron Devices and Solid State Circuits*, Hong Kong, June 2013.
- [2] S. Raju, R. Wu, M. Chan and C. P. Yue, "Modeling of mutual inductance for planar inductors used in inductive link applications," *IEEE International conference on Electron Devices and Solid State Circuits*, Bangkok, Thailand, Dec. 2012.
- [1] R. Wu, S. Raju, M. Chan, J. K.O. Sin and C. P. Yue, "Wireless power link design using silicon-embedded inductors for brain-machine interface," *International Symposium on VLSI Design, Automation and Test*, Hsinchu, Taiwan, April 2012.